# Self-Assembly of Nanoparticle Surfactants

Michael T. Lombardo

A thesis

submitted in partial fulfillment of the

requirements for the degree of

Master of Science in Chemical Engineering

University of Washington

2014

Committee:

Lilo D. Pozzo

John C. Berg

Qiuming Yu

Program Authorized to Offer Degree:

Department of Chemical Engineering

University of Washington

**Abstract**

Self-Assembly of Nanoparticle Surfactants

Michael T. Lombardo

Chair of the Supervisory Committee:
Associate Professor Lilo D. Pozzo
Department of Chemical Engineering

Self-assembly utilizes non-covalent forces to organize smaller building blocks into larger, organized structures. Nanoparticles are one type of building block and have gained interest recently due to their unique optical and electrical properties which have proved useful in fields such as energy, catalysis, and advanced materials. There are several techniques currently used to self-assemble nanoparticles, each with its own set of benefits and drawbacks. Here, we address the limited number of techniques in non-polar solvents by introducing a method utilizing amphiphilic gold nanoparticles. Grafted polymer chains provide steric stabilization while small hydrophilic molecules induce assembly through short range attractive forces. The properties of these self-assembled structures are found to be dependent on the polymer and small molecules surface concentrations and chemistries. These particles act as nanoparticle surfactants and can effectively stabilize oil-water interfaces, such as in an emulsion. In addition to the work in organic solvent, similar amphiphilic particles in aqueous media are shown to effectively stabilize oil-in-water emulsions that show promise as photoacoustic/ultrasound theranostic agents.

## Table of Contents

**List of Figures**

Figure

**List of Tables**

Table

**Acknowledgements**

I would like to thank Lilo Pozzo for her help and support over the last two years as my advisor. I could not imagine a better advisor whose expertise in the field is only rivaled by her support and caring for her students. I would like to thank my committee, Dr. John C. Berg and Dr. Qiuming Yu, for their fairness and gentleness during my exams. I would also like the thank my lab mates (past and present) for their help in the lab as well as their own personalities: Pablo de la Iglesia for letting me teach him how to ride a bike and for sharing his love of corgis with me, Greg Newbloom for our deep discussions about life and grapes (mostly grapes), Jeff Richards for dominating on the soccer field with me, Kiran Kanekal for graciously taking an endless stream of sarcasm from me without angry retribution, and Yuyin Xi for being the subject of potentially the funniest driving story I have ever heard. Additionally, I would like to extend my gratitude to the three undergraduates, Rainie Nelson, Jess Little, and Sim Yee Chen, with whom I closely worked for a year on the GAANN project and without whom we would not have done so well.

## Dedication

To my friends and family

## Chapter 1. Nanoparticle self-assembly

Whitesides et al. define self-assembly as "processes that involve pre-existing components (separate or distinct parts of a disordered structure), are reversible, and can be controlled by proper design of the components."[1] Key to this definition is that steady state positions are achieved by a balance between attractive and repulsive forces Therefore, covalently bonded reactions are not considered self-assembly mechanisms leaving weaker interactions such as van der Waals, electrostatic, or magnetic interactions to drive the organization. By tuning these types of interactions, particles or components can be arranged in specific ways. As technology has moved towards the nanoscale, new challenges in self-assembly are encountered and new techniques are developed.

### 1.1 Background

Nanoparticle self-assembly presents unique challenges and benefits compared to its macro and microscopic counterpart. The nanoscale is a vague term, but generally refers to length scales below 1 μm. However, most interesting phenoma only become present below about 100 nm. Below this length, materials can develop properties that deviate from those found in the bulk phase and the forces used for self-assembly at this scale can be significantly different. Bishop et al. wrote a detailed review on these forces and their role in self-assembly.[2] One example of the unique phenoma at the nanoscale is the behavior of iron nanoparticles that become superparamagnetic (no permanent magnetic field) instead of exhibiting ferromagnetic (permanent magnetic field) behavior as bulk iron does. This can be useful for applications such as magnetic resonance imaging (MRI) where iron particles can be manipulated by an external magnetic particles, but do not retain any permanent dipole.[3] Another interesting effect observed at the nanoscale is confinement effects. Confinement effects can be used in plasmonic

applications to confine and trap light near the surface of a particle or hole, causing an enhancement of the electromagnetic fields near the surface of that particle. This is useful for solar cell applications and detection techniques such as surface enhanced Raman spectroscopy (SERS).[4,5] One of the newest applications of nano-sized geometries and organization is meta-materials that exhibit negative indices of refraction.[6] This phenomena can be used for so-called "cloaking" applications where the light is bent around an object, thus making it appear invisible. Common geometries and particles are made with lithographic[7] and clustering techniques (discussed below).

### 1.2 Current Self-Assembly Techniques

With so many interesting properties and applications, one can surmise that there are numerous techniques currently used to self-assembly nanoparticles. Because there are so many, this thesis will focus on techniques that provide control over the assembly and ignore techniques that completely destabilize particle dispersions, such as adding salt to an electrocratic dispersion. Additionally, the focus will be on self-assembly into clusters and emulsions. There are several techniques used to produce non-cluster/emulsion geometries such as selective adsorption to form chains of gold nanorods[8] or utilizing the transient dipoles in gold particles to make chains[9], but these will also not be discussed here.

#### 1.2.1 Clusters

Clusters are aggregates of individual particles of two or more. They are typically 3 dimensional in organization as opposed to 1D (chains[9]) or 2D (lattices[10]) and often take on geometric configurations like tetrahedrons, trending towards spherical clusters as the number of particles increase. Several techniques for self-assembly of particles into clusters are reviewed nicely by Lu et al.[11] DNA linking uses complimentary base pairs to selectively link two DNA

strands together.[12] By functionalizing different particle populations with complimentary base pairs, self-assembly can be very effectively controlled. This is one of the most accurate methods for self-assembling particles, because the base pairs will not conjugate with uncomplimentary strands. Evaporation induced self-assembly (EISA) uses an emulsion based technique to force particles together.[13] By suspending the particles within an emulsion droplet, the particles can be forced to cluster simply by removing the solvent. Another technique quenches a slowly aggregating system with a polymer and can be used to selectively tune the average cluster size by trapping the aggregates in a block copolymer.[14] One recent technique developed by Larson-Smith et al. uses a balance of steric repulsion of long poly(ethylene glycol) chains and short range attraction for alkane thiols to induce self-assembly of gold nanoparticles.[15]

There are clearly many techniques for controlled self-assembly. However, each of these has their own advantages and disadvantages. DNA linking, for example, is very precise, but is prohibitively expensive for large scale production due to the cost of the DNA. EISA, while much more scalable and less expensive, is limited by the initial emulsion size, making small clusters difficult to produce. In addition to these types of tradeoffs, most of these techniques share one critical limitation: they must be performed in aqueous systems. Little work on self-assembly is done in organic solvent, and when organic solvents are used, they are typically polar solvents such as ethanol or tetrahydrofuran (THF). Examples of self-assembly in polar organic solvents include quenching of gold nanoparticle aggregation with an amphiphilic block copolymer in THF[16] or dimethylformamide (DMF)[14]. Unfortunately, the constituents used in these polar systems will not likely behave the same way in non-polar solvents. This means that applications which utilize low dielectric solvents such as toluene do not have a library of self-assembly techniques available to them. One application where this is relevant is in organic photovoltaics

(OPVs), which are often processed in non-polar organic solvents like dichlorobenzene. Because of the lack of techniques available, less scalable top down techniques such as lithography or liquid/vapor deposition techniques are often used.[4,17,18] The use of these expensive or inefficient techniques ultimately limits the prospect of bringing these new technologies to production due to high costs (material or processing).

### 1.2.2 Emulsions

Emulsions are droplets of one liquid in another in which neither are miscible with the other. The classic example is an oil-in-water emulsion (O/W) in which the dispersed phase is oil. Emulsions are used in several applications such as the food and oil industries[19,20] and more recently in drug delivery.[21] Emulsions without stabilizing agents tend to coalesce because they are thermodynamically unstable. By adding surfactants, the emulsions can be stabilized from coalescence due to the electrostatic repulsion of the charged surfactant heads. Molecular surfactants like sodium dodecylsulfate (SDS) are among the most common molecules used for stabilizing emulsions due to their tight packing and effective charge repulsion. Another type of stabilizing agent is solid particles. When particles stabilize an emulsion, it is called a Pickering emulsion.[22] Pickering emulsions are more stable than molecular surfactant stabilized emulsions because the energy required to desorb a particle from the interface is much higher than the thermal energy, kT, whereas molecular surfactants are constantly desorbing and adsorbing.[23] Unlike surfactants which are nearly always amphiphilic, homogeneous particles can be used to make Pickering emulsions.[24] This is because the particles stabilize the interface by reducing the interfacial energy. Recently, Janus particles have been used to create even more stable Pickering emulsions, some even to the point of thermodynamically stable.[25] These Janus particles self-

assembly at the interface much like a traditional surfactant due to their amphiphilic nature. Several types of Janus particles have been explored.[23,26]

There are a few unique challenges that arise when forming Pickering and traditional emulsions at very small scales. So-called nano-emulsions are those whose diameter is under about 200 nm. Their properties, applications, and synthesis techniques are outlined in several articles.[27,28] One of the key challenges in dealing with these small emulsions includes the dramatic changes in Laplace pressure when the radius of curvature becomes very small. As the particles decrease to very small sizes, the Laplace pressure can increase dramatically and increases the solubility of the dispersed phase in the bulk.[27] This leads to destabilization of the dispersion through Ostwald ripening.[29] Another challenge is successfully getting the particles to the interface before coalescence occurs. This is more challenging with larger particles than molecules due to their decreased mobility. Additionally, as the emulsion size becomes closer to the particle size, the packing at the interface can become an issue. One can imagine that it is difficult to surround a 30 nm droplet with 10 nm particles. Therefore, emulsion processing and long term stability are of great interest for these nanoscale emulsions.

**Chapter 2. Nanoparticle Characterization Techniques**

There are a number of techniques available to characterize nanoparticles. These techniques range from imaging techniques such as transmission electron microscopy (TEM), which provides pictures of the particles, to scattering techniques requiring data fitting. Depending on the nanoparticle being characterized and the information that is desired, different techniques may be more or less appropriate. One special property of the particles used in this work is their plasmonic behavior. Plasmonic paraticles are those that possess a delocalized electron cloud, such as in metals, which interacts with an incident electromagnetic wave, causing

a collective oscillation of these electrons. This oscillation creates a dramatic enhancement of the electromagnetic field near the particle surface and is called Localized Surface Plasmon Resonance (LSPR).[30] This enhancement causes dramatic increases in local electric field, which is advantageous for several applications like organic photovoltaics (OPV's) and surface enhanced Raman spectroscopy (SERS), discussed later. Below is a description of each technique used in the following work to characterize gold nanoparticles.

**2.1 UV-Vis Spectroscopy**

The optical and electronic properties of plasmonic particles are extremely interesting for applications such as wave guides[31], organic photovoltaics[17], and the design of metamaterials[6]. Due to the interest in controlling optical properties, which are often related to electronic properties, there is motivation to be able to measure these traits. By measuring the optical properties, one could conceivably change and tune parameters in order to optimize the system. One method to measure optical properties is UV-Vis spectroscopy.

UV-Vis spectroscopy is a light absorbance technique that irradiates a sample with light of a specific wavelength (ranging from about 200 nm – 1100 nm) and measures the amount of light transmitted through the sample. By measuring the transmittance at many wavelengths, one obtains a plot of wavelength in nanometers vs absorbance. Absorbance is calculated with the Beer-Lambert Law, commonly referred to as simply Beer's Law, presented in equation 2.1.1.

$$A = \varepsilon l c \qquad 2.1.1$$

A is the absorbance (unitless), ε is the absorptivity of the material, l is the pathlength that the light travels through the sample, and c is the concentration of the absorber.

Absorbance is related to transmission by the formula Light In = Light Absorbed + Light Transmitted + Light Scattered. For small plasmonic nanoparticles, the contribution from the

scattered light is generally small so the absorbed light is simply whatever light is not transmitted.[32] This is true for particles less than about 40 nm in diameter. Above that size, the scattering contribution becomes larger than absorbance.[32] Therefore, what is truly measured by the UV-Vis is better known as the extinction spectrum which is the sum of scattering and absorbance spectra. However, for the small particles used in this work, it is generally assumed that the extinction is dominated by absorbance.

For gold nanoparticles, the absorbance spectrum typically shows one predominant peak, which is representative of the characteristic diameter present in the particle population. For example, gold nanospheres between about 2-20 nm in diameter show an absorbance peak at 520 nm, while larger spheres have red shifted peaks. Nanorods on the other hand show two characteristic peaks, one at smaller wavelengths corresponding to the diameter and one at higher wavelengths corresponding to the length.[33]

Because larger length scales and structures absorb at higher wavelengths, the peak and shape of the absorbance curve can give information about the structures and sizes of particles or clusters present in the sample. A representative curve is shown in figure 2.1.1.

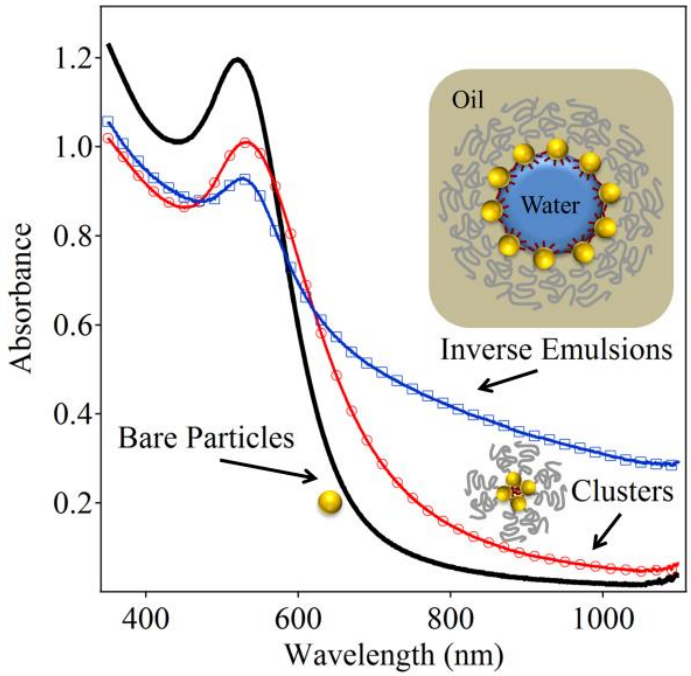


**Figure 2.1.1** UV-Vis absorbance curves for bare particles, clusters, and inverse emulsions.

Notice that the clustered sample has a red shifted peak and a broadened tail compared to the individual particles. This behavior can be used to indicate whether aggregation is present. Additionally, with great enough shifts, a visible change in color of the sample is observed, corresponding nicely to the change in absorbance. Furthermore, the particle organization can also affect the absorbance as is seen by the increase in NIR absorbance by an O/W emulsion decorated by gold nanoparticles. The organization of the particles as a shell results in a different absorbance spectrum than a cluster of particles the same size.

### 2.2 Dynamic Light Scattering (DLS)

As discussed above, the size of nanoparticles can be important for control of optical and other properties. Therefore, one would like a reliable method for characterizing the size. Additionally, particles are rarely all exactly the same size. Instead, there is typically a distribution ranging from relatively monodisperse (narrower distribution) to relatively polydisperse (wider distribution). The degree of polydisperity that is acceptable is dependent on

the experiment and application. For measurements where the total amount of particle mass is important, a polydisperse sample might be acceptable, whereas a study dependent on accurate measurement of the total available surface area might require a much narrower distribution.

DLS provides a method to measure particle size distribution in dispersion. It is advantageous over dried techniques such as TEM (described in section 2.3) because it measures the sample non-destructively and without any special sample preparation needed, except appropriate dilution. DLS uses a laser to measure scattering intensity. By measuring the intensity over time, a correlation curve is generated. This curve is a measure of how correlated the particles at time, t, are compared to some future time, $t+\delta t$. At short times, the particle positions are highly correlated, because the particles have not moved much, so the correlation function is close to 1. At long times, the particle positions are completely uncorrelated, so the function has a value that approaches 0. Due to Brownian motion, larger particles exhibit slower decreases in correlation than smaller particles. By fitting the correlation function to size distributions, the DLS data is presented in a valuable form as an intensity distribution fit. This fit represents the distribution of particle sizes that correspond to the percentage of total scattering intensity that is observed. For a bimodal or multimodal distribution, the relative height of the peaks relate to the percentage of intensity at those sizes. However, as scattering is a volume dependent phenomenon, the larger particles are weighted more heavily than smaller ones. So although the intensity may be larger for the distribution at a larger size, it is possible that the smaller sized particles are more numerous. This needs to be considered when analyzing DLS data as choosing the different distributions to look at can change the reported values. For this work, the volume distribution is used.

It should be noted that DLS measures hydrodynamic size, not actual size. The hydrodynamic size of a particle is its "effective" size in the solvent. In water, the effective size of particles can be larger than the real size due to the counter ion cloud, or double layer. The double layer is the layer of ions that are opposite in charge to the surface charge of the particle that move with the particle. It is well known that this double layer can change the mobility of a particle through effects such as retardation.[34] In DLS, the double layer decreases the speed of Brownian diffusion of the particle, which is what changes the correlation of the particles in time. Because the DLS uses the Stokes-Einstein equation to calculate the particle size, it assumes that the particles are spheres. This then results in the particle appearing larger because of its slower diffusion. Another, and more dominant, effect for increasing the effective size of a particle in DLS is the presence of bound surface ligands. These ligands increase hydrodynamic drag as the particle moves, slowing it down much like the double layer.

For particles with grafted polymer chains, the DLS is useful for determining the extension and conformation of the polymer.[35] The polymers slow down the particle the more extended in solution they are due to an increase in drag. These effects are demonstrated nicely by Larson-Smith et al. who shows that different polymer conformations are obtained when the polymer surface concentration and/or the density of the alkane thiol monolayer are changed.[35] These same principles apply to the non-aqueous system described in this work, although an in depth study of these effects is not performed. However, the data do suggest that similar effects are present.

**2.3 Transmission Electron Microscopy (TEM)**

Microscopy techniques provide images that are useful for confirming other measurements such as those from DLS. For nanoparticles, the TEM provides enough resolution to image

particles as small as about 1 nm when operated in normal mode. By providing images of the particles, it is easy to confirm or refute size distributions obtained through other means. As mentioned in section 2.2, TEM sample preparation requires drying the particles on a carbon coated copper mesh grid. This often results in a loss of information due to drying effects and loss of 3-dimensional information due to the projection of 3D objects on a 2D image, as well as collapse of 3D structures when the solvent is removed.

TEM uses high energy electrons to bombard a sample, so heavy elements such as metals show up well while polymers are difficult to distinguish against the carbon background. For the gold nanoparticles used in this work, contrast is high and it is easy to distinguish individual particles. Additionally, the polymer layer is not visible and only the particles result as shown in figure 2.3.1.

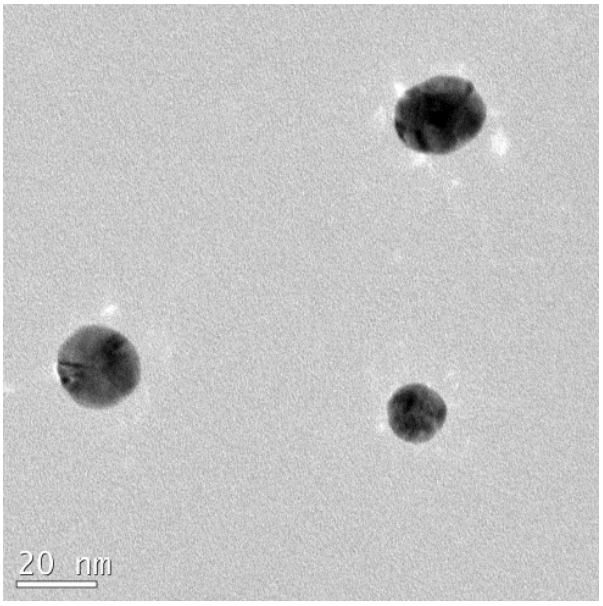


**Figure 2.3.1** TEM image of gold nanoparticles.

By analyzing images in ImageJ software, a particle size distribution is obtained. ImageJ is a free software program available online. Images are opened with the software and

subsequently smoothed. The smoothing evens the intensity of the pixels, which helps to eliminate the background noise into a flat background (Smoothed image in Figure 2.3.2 left).

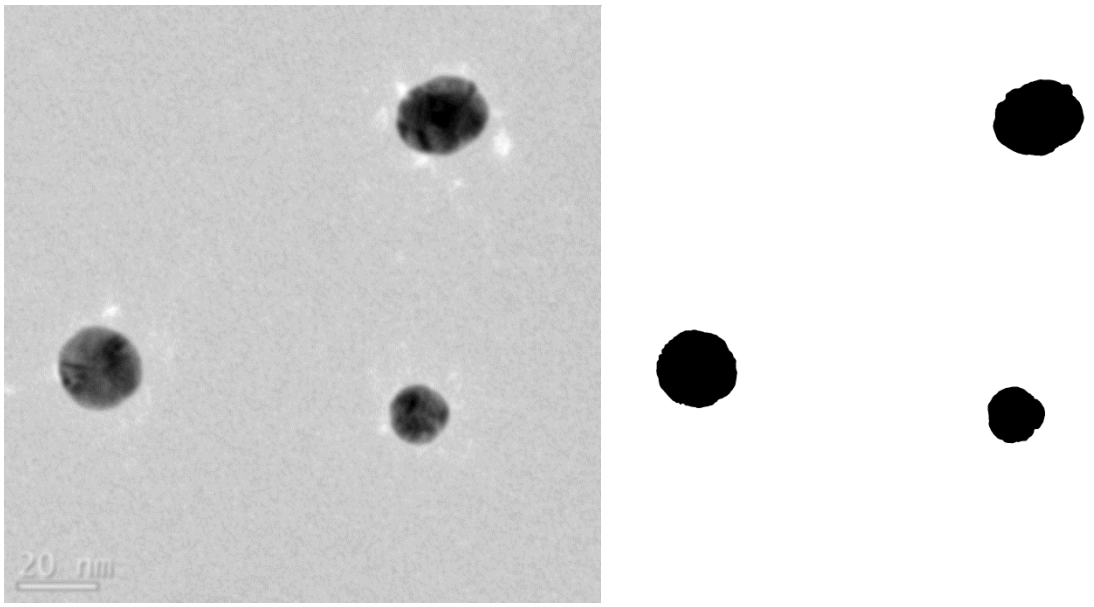


**Figure 2.3.2** Smoothed TEM image (left) and after threshold is applied (right)

After smoothing, the threshold function (figure 2.3.2 right) is used to highlight only the particles and then the particle sizes are calculated using the automatic "analyze particles" function. This function returns the area in pixels of each particle. In order to extract a particle size in useful units, one must correlate the pixel size to a length. This is done by measuring the length of the scale bar and calculating the number of pixels per nm. This can then be used to convert the area into $nm^2$, which is then used to obtain the diameter or radius. By repeating this process for a large number of particles, a rather accurate size distribution is obtained, which is most often confirmed with SAXS for individual particles. A key aspect of the sample preparation is to dilute the samples such that particles are not overlapping since the software cannot distinguish between touching particles. This concentration is given in the following Methods sections. For clusters and emulsions, dispersions must be diluted even more in order to negate

drying effects. These effects, such as the coffee ring effect, can pull clusters close together as the volume of solvent is lost to evaporation. If the sample is too concentrated, it is difficult if not impossible to distinguish between clusters formed due to self-assembly in dispersion and which were aggregated during grid preparation.

**2.4 Thermogravimetric Analysis (TGA)**

As materials are heated, they will all eventually reach a decomposition temperature. This is the temperature at which the bonds are broken and the material decomposes into constituent components. A classic example of decomposition is of calcium carbonate into calcium oxide and carbon dioxide. For the decomposition of polymers, the products are dependent on the chemical structure. For poly(ethylene glycol) (PEG), the major decomposition products are ethanol, methanol, alkenes, non-cyclic ethers, formaldehyde, acetic aldehyde, ethylene oxide, water, carbon monoxide, and carbon dioxide.[36]These products can be analyzed by sending the decomposition gas through an FTIR or mass spectrometer.

TGA is a technique which measures the change in mass of a sample over time. It is essentially a microbalance with a heater that allows the user to change the sample temperature in a number of ways (i.e. ramp, isothermal, step change, etc.). In multicomponent systems, TGA can be used to determine composition and also the effect of different heating rates or temperature conditions on the substance.

In this work, TGA is used to determine the polymer surface concentration. In a given run, both the polymer mass and gold mass are obtained as shown in figure 2.4.1.

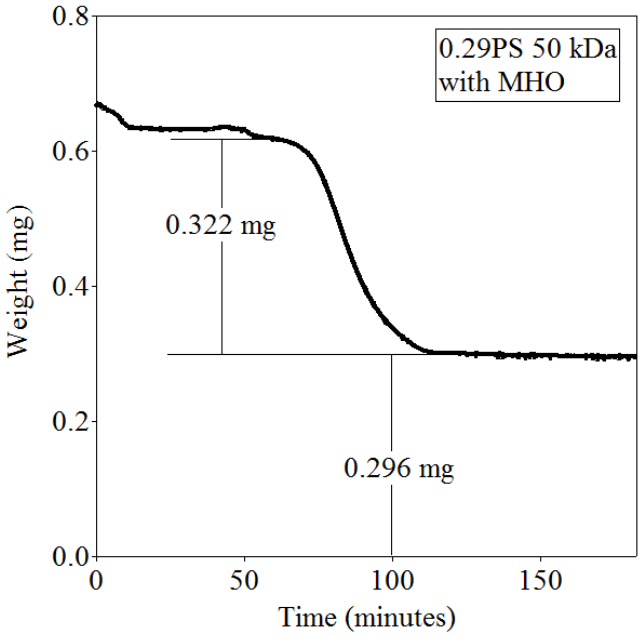


**Figure 2.4.1** Sample TGA curve.

The polymer mass is given by the first drop in mass marked by 0.322 mg. This mass is converted to moles and subsequently, the total number of polymer chains. The gold mass is assumed to be whatever remains in the pan at the end of the run, which in this case is 0.296 mg. By using the average particle size, the total surface area of gold can be calculated and, assuming even coverage, the number of chains / $nm^2$. This calculation is most accurate when larger masses are used as the instrument tends to drift and show noisy results below 0.1 mg of sample. Thus, samples of >0.6 mg were typically used and provided reproducible results. It is difficult to distinguish between the small thiols and the polymer because both have similar compositions. However, the maximum mass of thiol capable of adsorbing on the surface is so low (0.007 mg) that the mass of the polymer dominates and the thiol mass is negligible for the preparation techniques used here.

## 2.5 Small Angle x-Ray Scattering (SAXS)

SAXS is an especially useful technique to non-destructively probe the structure of a sample in a dispersion or solution. Unlike diffraction or wide angle scattering techniques, which

look at Ångstrom scale parameters, small angle scattering focuses on larger length scales on the order of a few nanometers up to several tens of nanometers. The upper end of this range is determined by the alignment of scattering instrument. A detailed look at scattering techniques and theory is give in several resources and the below sections will describe the relevant theory to the work presented in this thesis.[37,38]

### 2.5.1 Fundamental SAXS Principles and Equations

A schematic of the setup for a SAXS instrument is shown in figure 2.5.1.1.

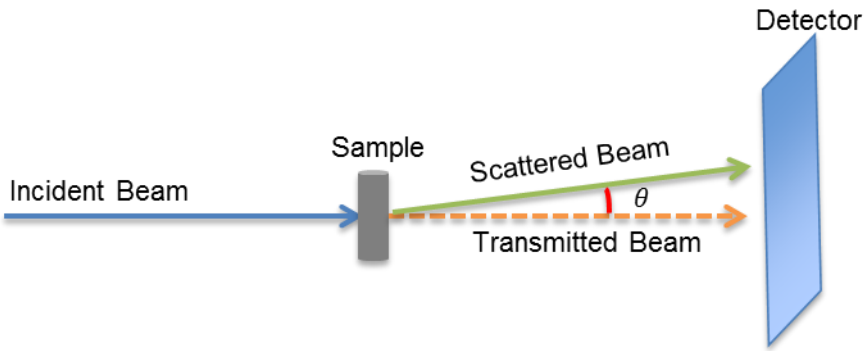


**Figure 2.5.1.1** Schematic of SAXS.

When the incident beam strikes the sample, some of the x-rays are transmitted and others are scattered at an angle θ. For SAXS, interactions with the sample are considered to be elastic, so no energy is transferred between the sample and beam. Other techniques such as quasi-elastic neutron scattering (QUENS) take into account and measure the energy transferred. For line collimated systems, the 2-dimensional scattering pattern is reduced to a 1D profile by averaging over the horizontal dimension (along the beam). Once this is done, the difference between the scattered beam and the transmitted beam can be measured and is called the scattering vector, q, whose magnitude is given by equation 2.5.1.1 where θ is the scattering angle and λ is the wavelength of the beam.

$$q = \frac{4\pi}{\lambda}\sin\left(\frac{\theta}{2}\right) \qquad 2.5.1.1$$

Because scattering is an inverse technique, q has units of reciprocal length, typically $Å^{-1}$. Therefore, features at low values of q represent larger length scales and high values of q represent small distances. Diffraction techniques look at high q values while small angle techniques look exclusively at low values of q.

Due to the slit collimation of the x-ray instrument, the measured scattering data is smeared. This can be corrected by either desmearing the data or by smearing the models. The model fitting software (SASView) developed at NIST can take the beam height calculated from the beam profile and automatically smears the models for fitting.[39] The slit collimation is used to increase the overall flux of x-rays so that count times are reduced.

The interaction of x-rays with atoms is through their electron cloud. Therefore, atoms with many electrons (metals) will scatter more effectively than atoms with fewer electrons (hydrocarbons). To quantify the difference is scattering capabilities between atoms, a term called scattering length density (SLD), ρ, is created and is defined in equation 2.5.1.2 for an $A_mB_n$ molecule.[37] It is the ratio of the scattering length per molecule and the molecular volume where v is the molecular volume, b is the scattering length of each atom, and m and n are the number of each atom in the molecule.

$$\rho = \frac{mb_A + nb_B}{v} \qquad 2.5.1.2$$

The scattering length of an atom is the apparent size of that atom to the incident radiation and has units of length. This is a measurable quantity and is related to the index of refraction, n, and the atomic density, ρ, through the following relationship in equation 2.5.1.3.[37]

$$n = 1 - \frac{\rho b}{2\pi}\lambda^2 \qquad 2.5.1.3$$

The scattering intensity of a sample is a function of the contrast in SLD's of the different components. This difference, often referred to as $\Delta\rho^2$ is given by

$$\Delta\rho^2 = (\rho_A - \rho_B)^2 \qquad 2.5.1.4$$

where ρ is the SLD of compounds A and B. For gold ($\rho_{Au}$=0.000125 $cm^{-1}$) in most common solvents, the contrast is typically around 2 orders of magnitude. This contrast is much greater than for a polymer and solvent (much less than 1 order of magnitude) so the polymer is effectively invisible compared to the gold and is neglected when models are used. This means that SAXS can be used to probe only the structure of the gold in the gold/polymer system of this work. For information about the polymer, neutron scattering is the preferred method and several models have been used to study grafted polymer chains on spheres.[40–43]

### 2.5.2 Models and Fitting

*Sphere Model*

The sphere model was derived by Guinier in 1955 and is one of the most fundamental models in scattering.[44] Because the gold synthesis techniques used in this work result in highly spherical particles, this is an excellent model to use and provides very accurate fits. The equation for the scattering of a sphere is presented in equation 2.5.2.1 where *vol frac* is the volume fraction of the scattering objects (in this case gold spheres), *V* is the volume of the scattering object, *r* is the radius of the sphere, *Δρ* is the difference is scattering length density between the scattering object and the solvent, and *q* is the scattering vector.

$$I(q) = \frac{vol\ frac}{V}\left[\frac{3V(\Delta\rho)[\sin(qr) - qr\cos(qr)]}{(qr)^3}\right]^2 + background \qquad 2.5.2.1$$

When fitting to this equation, the SLD's of gold and the solvent are known and are held constant. Additionally, an initial guess of the particle size can be input from other characterization techniques such as TEM or DLS. The predominant value obtained by the fit is

the volume fraction of gold, but the particle size is also allowed to vary in order to confirm the size obtained from TEM. The fitting is done using SASView software.[39]

*Raspberry Model*

Pickering emulsions are emulsion droplets decorated with solid particles and was first described by Spencer Pickering in 1907.[22] Larson-Smith et al. derived a small angle scattering model for this structure (also raspberry particles, or a large particle decorated by smaller particles) and the details of the derivation are laid out nicely in their publication.[45] The equation used to fit monodisperse Pickering emulsions is given by equation 5.2.5.2.

$$I_{Total}^{Mono}(q) = I_{Total}^{Mono}(q) + I_{p}^{Mono}(q) \quad 2.5.2.2$$

$$I_{Total}^{Mono}(q) = \left(\phi_o(\Delta\rho_o)^2 V_o + \phi_p^T \phi_p^a N_p \left(\Delta\rho_p\right)^2 V_p\right) P_{op} \quad 2.5.2.3$$

$$I_{p}^{Mono}(q) = \phi_p^T (1-\phi_p^a)\left(\Delta\rho_p\right)^2 V_p \Psi_p^2 \quad 2.5.2.4$$

$P_{op}$ (equation 2.5.2.5) represents the form factor of the emulsion+particle complex and M (equation 2.5.2.6) gives the scattering length.

$$P_{op} = \frac{1}{M^2}\left[(\Delta\rho_0)^2 V_0^2 \Psi_0^2 + N_p\left(\Delta\rho_p\right)^2 V_p^2 \Psi_p^2 + N_p\left(N_p-1\right)\left(\Delta\rho_p\right)^2 V_p^2 S_{pp} + 2N_p \Delta\rho_0 \Delta\rho_p V_0 V_p S_{op}\right] \quad 2.5.2.5$$

$$M = \Delta\rho_0 V_0 + N_p \Delta\rho_p V_p \quad 2.5.2.6$$

$$N_p = \frac{\phi_p^T \phi_p^a V_0}{\phi_0 V_p} \quad 2.5.2.7$$

$$\Psi_p^2 = \frac{3[\sin(qR_p) - qR_p\cos(qR_p)]}{(qR_p)^2} \quad 2.5.2.8$$

$\phi_p^T$: volume fraction of particles
$\phi_0$: volume fraction of emulsion phase
$\phi_p^a$: fraction of total particles adsorbed at the interface
$N_p$: number of particles at the surface of a single emulsion
$V_0$: volume of a single emulsion drop
$V_p$: volume of a single solid particle
$\rho_0$: scattering length density of the emulsion phase

$\rho_s$: scattering length density of the solvent
$\rho_p$: scattering length density of the small particles
$\Delta\rho_0$: contrast of emulsion phase with solvent $= |\rho_0 - \rho_s|$
$\Delta\rho_p$: contrast of particles with solvent $= |\rho_p - \rho_s|$

For all fitting, the sphere penetration depth is held at zero. This is because it is found to have a negligible effect when the emulsion is much larger than the particles.[45] The SLD's are also held constant because they are known values.

## Chapter 3. Clusters and Inverse Emulsions from Nanoparticle Surfactants in Organic Solvents

The work present in this chapter is submitted to *Langmuir* (Dec. 214).

### 3.1 Introduction and Background

Nanoparticle clusters are used in a number of applications such as photothermal therapy[46], bioseparations[47], and imaging[48]. One advantage of metal clusters is that they can exhibit different optical properties than their individual building blocks due to overlap of their plasmon resonance. By placing gold surfaces close together, the surface plasmons create "hot-spots" of large electromagnetic field enhancment.[30] This phenomena is utilized in surface-enhanced Raman spectroscopy (SERS) to provide signal enhancement on order of $10^6$, which allows for detection of extremely dilute compounds.[5] Another advantage is that both orientation dependent and independent properties can be achieved.[14] Orientation-independent optical properties resulting from tetrahedral configurations of plasmonic particles have been shown to be useful in applications such as meta-fluids with negative indices of refraction.[6] The tetrahedral configuration leads to clusters that interact with light in the same way regardless of orientation with respect to the incident light. This is advantageous for meta-fluids because the particles are in constant motion and their orientation with the incoming light is not easily controlled. Though much work has been performed to self-assemble particles in water, much less research has been

pursued for self-assembly in organic solvents. Moreover, much less has been reported for self-assembly in apolar organic solvents, which is be the focus of this work.

There are several techniques used to create nanoparticle clusters (i.e. aggregates of 2 or more particles) and these are outlined nicely in a recent review by Lu and coworkers.[11] Many of these techniques suffer from drawbacks in terms of cost, versatility, scalability, and/or control of cluster size and shape. The most promising techniques can be classified as bottom-up assemblies that are advantageous over top-down methods (e.g. lithography) because less material is wasted, length scales are determined by the size of the building blocks, and the materials can be processed in bulk quantities. For example, accurate and reproducible particle clusters have been successfully produced through grafting complimentary strands of DNA onto gold nanoparticles to induce clustering.[12] This technique, however, is limited to aqueous systems because DNA hybridization is limited to polar solvents. It is also rather expensive due to the high costs associated with producing synthetic DNA. Another technique, evaporation induced self-assembly, creates clusters by forcing the aggregation of particles that are confined within an emulsion droplet upon the evaporation of the dispersed liquid phase. This technique is significantly more scalable than DNA grafting, but it is limited by the size of the initial emulsion. It is therefore difficult to achieve structural control over nanometer sized clusters.[13]

Recently, our group developed an inexpensive and scalable technique utilizing non-specific interactions to controllably form clusters of gold nanoparticles in water.[15] This technique renders 12 nm gold particle spheres amphiphilic through the sequential conjugation of long PEG chains and short alkane thiol molecules to the particle surface. By controlling the amount of PEG and the length of the alkane thiol, the cluster size is tunable to between 1-9 particles/cluster.[35] This work demonstrates an ability to controllably self-assemble particles in water without the use

of expensive raw materials, in a scalable fashion and with good control over the final cluster size. Water-based nanoparticle surfactants are also capable of stabilizing oil-in-water emulsions that have been recently demonstrated for use in photoacoustic imaging[49] and, potentially, in thrombolytic therapy[50]. Moreover, since this simple approach relies on the balance of repulsion from polymers and short-range attraction from alkane thiols, it should also be possible to extend this approach to non-polar organic solvent systems.

Controlled self-assembly in organic solvents can be useful for a number of applications where processing takes place in non-aqueous media. Organic photovoltaics, for example, have shown improved efficiencies when plasmonic particles are added into the active layer of devices, which is processed from organic solvents.[17] Small plasmonic particles, such as gold and silver spheres, increase device absorption efficiency through the coupling of their localized surface plasmon resonance (LSPR) with the surrounding active layer.[51] Clusters of plasmonic spheres show even larger LSPR enhancement than individual particles through the formation of so called "hot spots", where the LSPR fields between particles overlap, generating large field enhancements. Self-assembled clusters could therefore be used to optimize and improve device performance by controlling both the particle and cluster size. Particles can also improve device efficiency when deposited just outside of the active layer.[52] One method of deposition for such an application is via the Langmuir-Blodgett technique.[53] Chen et al. show that the packing structure of gold particle arrays on a substrate by this method can be altered through the manipulation of the surface pressure within a thin layer of particles in organic solvent that is spread over a water subphase.[53] Upon evaporation of the solvent, the particles are transferred onto the substrate yielding an organized array for use in an organic solar cell. It is likely that this

and other processes could be simplified by using surface-active particles, such as those presented in this work, to adsorb at the interface.

Other techniques for cluster self-assembly in organic solvents have also been reported to yield precise control of size and shape. One such study successfully controls the chain length of linearly aggregated gold nanoparticles in ethanol by controlling the particle concentration.[9] Further insight on linear assembly of charged nanoparticles in polar organic solvent (e.g. ethanol) is given by Han et al. who elucidates the role of salt in nanoparticle aggregation in these systems.[54] Another group reports clusters of polystyrene functionalized spherical gold nanoparticles in tetrahydrofuran (THF) formed with the addition of water followed by quenching of cluster growth with an amphiphilic block copolymer (e.g. polystyrene-*block*-polyacrylic acid), making them stable in water.[16] Using this same fundamental technique, Urban et al. obtain precise control over the 3-dimensional cluster geometry of gold nanoparticles.[14] In addition to model gold nanoparticle systems, self-assembly in organic solvents is also achieved for Pd nanoribbons in a toluene/THF solvent.[55] Although each of these techniques demonstrates self-assembly in organic solvents, it is clear that most of the work in this field utilizes polar solvents such as water and alcohols and not low-dielectric constant apolar solvents such as toluene.

Here, we demonstrate the extension of a scalable and inexpensive method for controllably self-assembling amphiphilic nanoparticle surfactants synthesized in organic solvent into clusters and inverse emulsions.[15] Gold nanoparticles 3 nm in diameter synthesized in toluene are rendered amphiphilic by conjugating the surface with long polystyrene chains and short, hydroxy or carboxylic-acid terminated alkane thiol molecules. The polystyrene chains provide steric stabilization, preventing uncontrolled aggregation, and the short hydrophilic molecules induce attraction and self-assembly. By manipulating the polymer molecular weight (MW) and

surface concentration, and by selecting small molecules with various chemistries, different cluster sizes are formed and long term stability is controlled. In addition, the amphiphilic nature of the particles is exploited to show that they act as nanoparticle surfactants to stabilize water-in-oil emulsions which could be used for templating of micro and nanoporous materials.[56] A powerful implication of this work is that it demonstrates the generality of this self-assembly technique. By carefully selecting the polymer/solvent combination and appropriate small molecules, this technique of balanced steric repulsion and short-range attraction can likely be translated to other solvents, particles, and polymer systems.

### 3.2 Experimental Methods

*Materials*

Gold chloride trihydrate, tetraoctylammonium bromide (TOAB), sodium borohydride, Mercaptooctanoic acid (MOA), 6-Mercapto-1-hexanol (MHO), and 6-Mercaptohexanoic acid (MHA) are purchased from Sigma Aldrich (St. Louis, MO) and are used as received. Thiol-terminated polystyrene (PS) (20kDa Mw/Mn=1.07 and 50kDa Mw/Mn=1.06) is purchased from Polymer Source (Dorval (Montreal), Quebec, Canada) and is used as received.

*Synthesis of Nanoparticle Surfactants*

Gold particles (3 nm in diameter) are synthesized in toluene following the method originally outlined by Brust[57] with TOAB acting as the phase-transfer agent and also as the only stabilizing agent. This reduces particle monodispersity from that which is usually achieved when synthesis occurs in the presence of thiol capping agents. However, this compromise is necessary in order to control surface functionalization independent of the particle synthesis steps. In this synthesis, 10 mL of 0.025 M $HAuCl_4$ in water is combined with 25 mL of 0.05 M TOAB in toluene is mixed in a 125 mL separation funnel. The aqueous phase is removed and the organic

phase which now contains the gold is transferred to a 125 mL Erlenmeyer flask. This solution is heated until it boils while vigerously stirring. Once boiling, 10 mL of 0.4 M $NaBH_4$ in water is added at once. After 15 minutes, the reaction is over and the separation funnels is used to isolate the organic phase. The volume fraction of gold particles is $2.3 \cdot 10^{-4}$. Glassware cleanliness is extremely important and therefore the glassware is soaked in NoChromix solution overnight. Appropriate safety precautions must be taken for this cleaning solution. The particles are subsequently functionalized with the addition of a controlled amount of mono-thiolated polystyrene at concentrations corresponding to 1 or 10 chains / $nm^2$ of gold surface area. After the polymer addition, the dispersions are allowed to sit for at least 4 days to allow the polymer to fully bind. However, not all of the polystyrene is expected to bind to gold particle surfaces because of the limited reactivity and steric repulsion with neighboring chains. This results in surface concentrations of 0.31 chains / $nm^2$ for PS 20 kDa loaded at 1 chains / $nm^2$, 0.86 chains / $nm^2$ for PS 20 kDa loaded at 10 chains / $nm^2$, and 0.29 chains / $nm^2$ for PS 50 kDa loaded at 1 chains / $nm^2$ of gold surface area as determined by TGA (Appendix). When functionalized with short thiols, the surface concentration is further reduced, and for MHO corresponds to 0.14 chains / $nm^2$ for PS 20 kDa loaded at 1 chains / $nm^2$, 0.43 chains / $nm^2$ for PS 20 kDa loaded at 10 chains / $nm^2$, and 0.25 chains / $nm^2$ for PS 50 kDa loaded at 1 chains / $nm^2$ of gold surface area. This reduction in surface concentration of polymer with the addition of short thiol has been observed in a similar system in aqueous media.[35] For simplicity, in this work we indicate polymer surface concentration and molecular weight using the following nomenclature XPS Y kDa, where X is the actual surface concentration before addition of small thiol in chains per $nm^2$ of available gold surface area and Y is the molecular weight. Unless noted otherwise, 'free' or un-bound PS is not removed from the dispersion because it is found to not induce any clustering

on its own. This is evaluated through both TEM and SAXS where it is found that aggregation does not occur after functionalization with just the polymer. The stock dispersion of polymer-functionalized particles is diluted by a factor of 21 before functionalization with the short thiol molecules. MOA, MHO or MHA molecules are added in great excess of >500 chains per $nm^2$ of available gold surface area. This is done to ensure that all the surface bound TOAB is replaced and the gold particles are fully coated with ligands. Despite the excess amounts, the expected maximum surface concentration of short thiols is only about 3-6 chains per $nm^2$ of gold surface area.[58,59]

*Emulsions*

To generate inverse emulsions, 0.31PS 20 kDa particles are centrifuged for 5 minutes at $14.8 \cdot 10^3$ $min^{-1}$ to remove large particles. The supernatant is then diluted with toluene to $6.9 \cdot 10^{-5}$ volume fraction of gold particles and then functionalized with MOA to render the particles amphiphilic. After 15 minutes, 10 μL of water is added to 1 mL of MOA functionalized gold dispersion and the mixture is sonicated with a Branson Digital Sonifier with a tapered 1/8" microtip at 10% amplitude, 1 second on, 3 seconds off, for 1 minute. Pulsing is used to minimize evaporation and heating of the dispersion which could cause a loss of the small volume of water that is added, thus changing the overall composition of the dispersion.

*Thermogravimetric Analysis (TGA)*

To determine polymer surface concentration, 250 μL of polymer-coated particles are deposited into a 1.5 mL centrifuge vial which is filled with methanol. Methanol is added to induce crashing of the clustered particles so that they could be collected at the bottom of the vial. The samples are then centrifuged at $14.8 \cdot 10^3$ $min^{-1}$ for 5 minutes. The liquid is decanted while making sure to leave enough to keep the gold from drying and the process is repeated so that a

total of 1 mL of gold dispersion is centrifuged to the bottom of the vial. After decanting for the second time, 1 mL of acetone is added to wash away any residual polystyrene from the solids. The vial is centrifuged again, the clear solvent is decanted, and this is repeated for a total of 4 acetone washes. The particles are then carefully transferred to aluminum TGA pans for measurement of total organic mass. Samples are run in a TA-Q50 (TA Instruments, New Castle, DE) with an initial isothermal segment at 115 °C for 30 minutes to remove any remaining solvent. The sample is then ramped from 115 °C at 10 °C/min to 400 °C and held for 2 hours to decompose all organic material. The purge gas is nitrogen at a flow rate of 60 mL/min. The run ended when the mass no longer changed indicating that all organic materials had been removed.

To determine the polymer surface concentration after MHO addition, 500 μL of polymer-coated particles are deposited into a 1.5 mL centrifuge vial to which 1 μL of MHO and 750 μL of methanol is added, in that order. Methanol is added to induce crashing of the clustered particles so that they could be collected at the bottom of the vial. The rest of the procedure is the same as described above. Although there is no way to discriminate between the contribution of MHO and the PS in TGA runs, the maximum mass (0.007 mg) of MHO that would be measured even if all of the gold surface is bound at ~ 3 chains / $nm^2$ is negligible compared to the total mass of gold and polymer (~ 1 mg total).

The mass of the polymer is converted to number of polymer chains and is divided by the total surface area of gold calculated from the gold mass remaining in the pan after each run using the known average particle size.

*UV-Vis*

Absorbance spectra are obtained with a Thermo Scientific (Waltham, MA) Evolution 300 system. Clustered samples are run at a volume fraction of gold of $1.1 \cdot 10^{-5}$ and emulsions are diluted to $3.3 \cdot 10^{-5}$. Both are measured in a 1 cm path length glass cuvette at room temperature.

*Dynamic Light Scattering (DLS)*

DLS measurements are performed on a Malvern Instruments (Worchestershire, United Kingdom) Zetasizer Nano HT using a 1 cm path length glass cuvette, 633 nm wavelength laser, and correlation times of 10 seconds for clusters and 1 minute for emulsions. The concentrations are the same as for UV-Vis.

*Small Angle X-Ray Scattering (SAXS)*

SAXS is performed with an Anton Paar (Graz, Austria) SAXSess equipped with a 1.54 Å CuKα x-ray source. Scattering patterns are collected on image plates that are processed with a PerkinElmer (Waltham, MA) Cyclone Plus. Due to approximately two orders of magnitude difference in scattering length densities of gold (Scattering Length Density (SLD) = $1.25 \cdot 10^{-4}$ Å$^{-2}$) and polystyrene (SLD = $1.41 \cdot 10^{-6}$ Å$^{-2}$) when compared to toluene (SLD = $8.03 \cdot 10^{-6}$ Å$^{-2}$), the SAXS data is largely representative of the relative position of nanoparticles within clusters because gold will be the dominant scattering object. Clustered samples are run at the same concentration as UV-Vis and inverse emulsions are run at a gold volume fraction of $6.9 \cdot 10^{-6}$. Scattered x-rays are collected on an image plate that is analyzed with the OptiQuant (PerkinElmer) software. Subsequent data reduction is performed in SAXSQuant 2D (Anton Paar) and SAXSQuant 3.70 (Anton Paar). The data reduction procedure accounts for background contributions from the cell and solvent. Data is put into absolute scale by measuring water as a

standard and using the known scattering cross section of water (0.01641 $cm^{-1}$). Fits are performed using the data analysis software SASView with smeared models.[39]

*Transmission Electron Microscopy (TEM)*

TEM images are taken on an FEI (Hillsboro, OR) Tecnai G2 F20 TEM at 200 kV. Images are processed with the ImageJ software. Pelco TEM grids are purchased from Ted Pella Inc (Redding, California). These are 400 mesh ultrathin carbon with one Formvar coated side. To prepare samples, dispersions are further diluted by a factor of 10 so that capillary aggregation due to drying would be negligible. This assured that clusters in TEM images are representative of isolated clusters found in dispersion. Due to the removal of solvent in TEM, all clusters tend to collapse and lose their original geometric configuration, which might be different in dispersion.[15] Therefore, TEM is principally useful in the assessment of cluster size, although geometrical configuration is lost due to collapse. This is also true for emulsions since there can be substantial collapse of 3D spheres when both fluid phases are removed. TEM grids for emulsions are also prepared without dilution because the concentration is already quite low making it difficult to locate emulsion beads in the grids. Drying effects did not appear to significantly influence emulsion images as indicated by comparison to samples that are frozen before deposition (Appendix).

**3.3 Results**

The UV-Vis absorbance spectra of bare particles, clusters, and inverse emulsions are shown in Figure 3.3.1 with schematics corresponding to the respective curves. The features of the absorbance spectra that indicate different forms of self-assembly include the peak shift to higher wavelengths and the broadening of the tail into the near-infrared (NIR) region.[60]

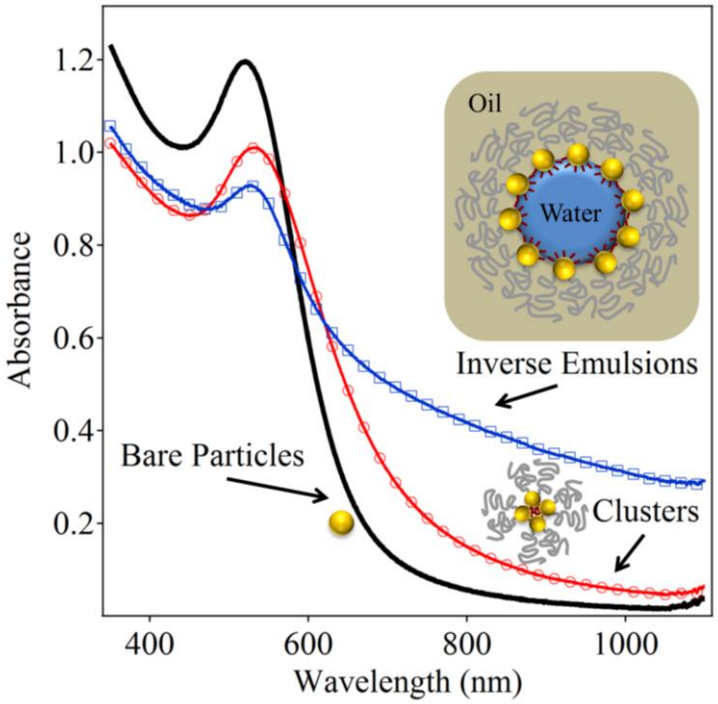


**Figure 3.3.1.** UV-Vis absorbance curves of bare particles, particle clusters made with MOA with a loading of 0.31PS 20 kDa, and inverse emulsions made with of 1 vol% water made with the clusters of 0.31PS 20 kDa loaded particles and MOA. Schematics are visual representations corresponding to the particle organization of each absorbance curve.

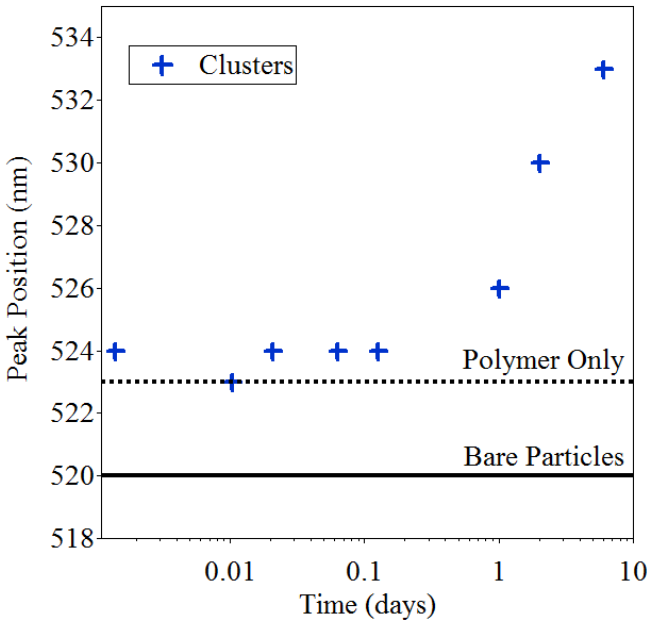


**Figure 3.3.2.** UV-Vis absorbance peak positions of 0.31PS 20 kDa loaded particle clusters vs time after clustering is induced (functionalization with MOA). Bare particles, particles with only

polymer at the above loading, and inverse emulsions are shown with horizontal lines for comparison.

Figure 3.3.2 shows absorbance peak position vs time after clustering for the 0.31PS 20 kDa. The characteristic peak at 520 nm for individual gold particles is shown and a red shift when the particles are functionalized with polystyrene is also observed. This shift upon polymer functionalization is due to the change in local refractive index (toluene = 1.496; polystyrene = 1.59) around the particle and does not indicate any type of aggregation. This fact is confirmed with TEM and SAXS measurements. Upon addition of the MOA, a systematic red shift of the peak position during the clustering process is observed. For this sample, clustering did not become significant enough to detect in the UV-Vis until about 1 day. The peak shifts steadily until the last data point is taken at 7 days.

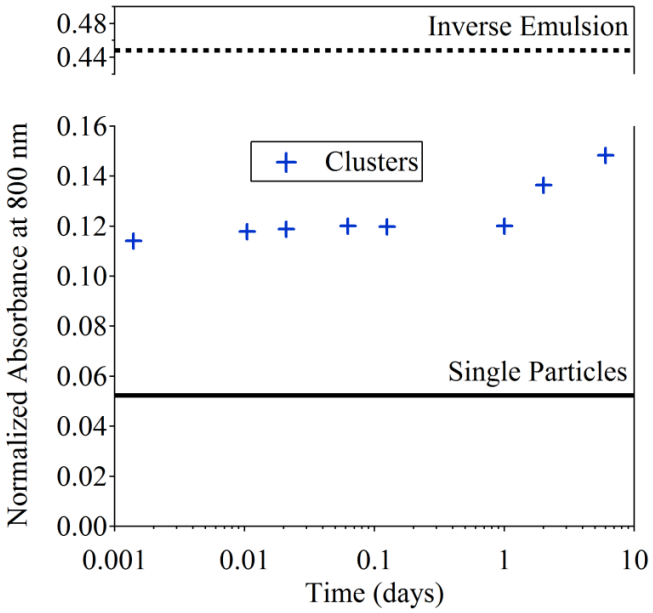


**Figure 3.3.3.** Peak normalized absorbance values at 800 nm for single particles functionalized with 0.31PS 20 kDa, clusters of the same loading with MOA, and inverse emulsions.

Another indicator of self-assembly is the broadening of the tail seen in figure 1 for the clusters and emulsion. In figure 3.3.3, the normalized absorbance value at 800 nm is plotted for single particles, clusters, and inverse emulsions. However, there is again a much more drastic

increase after one day for this measurement, which supports the peak shift trend of a slowly aggregating system. The emulsions show significantly more absorbance at 800 nm than the clusters and bare particles.

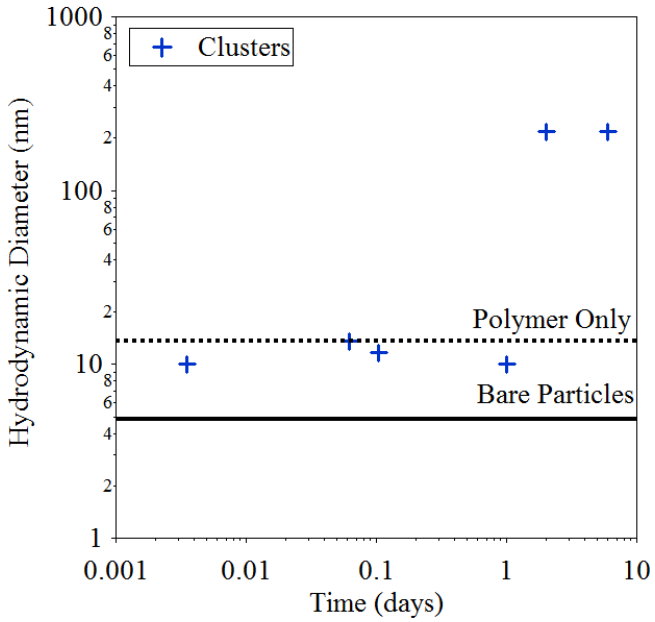


**Figure 3.3.4.** Hydrodynamic diameter obtained by DLS of 0.31PS 20 kDa loaded particle clusters over time with bare particles, polymer only particles, and inverse emulsions for comparison.

The pattern of increasing size over time is confirmed in the DLS data shown in Figure 3.3.4. The bare particles have a hydrodynamic diameter of 4.9 nm (volume fit). With the addition of the polymer, the diameter increases to 13.5 nm (volume fit). As seen in UV-Vis and TEM, the average size of the clusters increases with time during the clustering process.

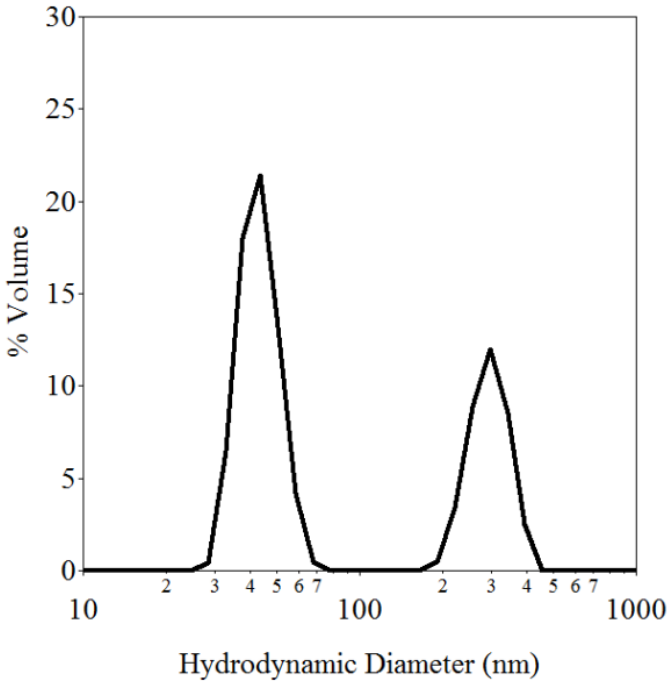


**Figure 3.3.5.** Hydrodynamic diameter (volume distribution) of inverse emulsions formed with 1PS 20kDa coated particles functionalized with MHO.

Figure 3.3.5 shows the size distribution of inverse emulsions. The distribution shows two populations. The population of smaller emulsions is centered at 44 nm and the larger emulsions are centered on 295 nm. These are known to be emulsions because, in addition to the TEM, SAXS, and UV-Vis evidence, a control was made from the same formulation but without the addition of water. The resulting clusters exhibited lower absorbance in the NIR and the DLS size was found to be smaller (centered at 21 nm) than the emulsions (Appendix).

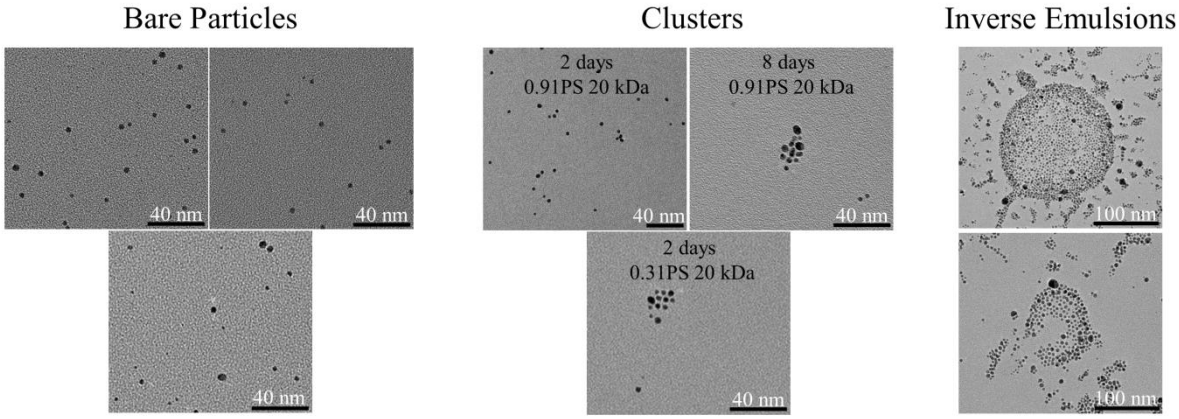


**Figure 3.3.6.** TEM images of bare particles as synthesized (left), clusters (center), and inverse emulsions (right).

Figure 3.3.6 shows representative TEM micrographs of the as synthesized particles, clusters, and emulsions. Although only a few examples are shown, many images were taken and used to determine the size distribution of the bare particles and to give a representative picture of degree of aggregation and emulsion size. The clustered samples show comparisons of 0.91PS 20 kDa samples functionalized with MOA at 2 and 8 days as well as a comparison at 2 days to 0.31PS 20 kDa. The emulsion images show two emulsion drops corresponding to the two different size distributions.

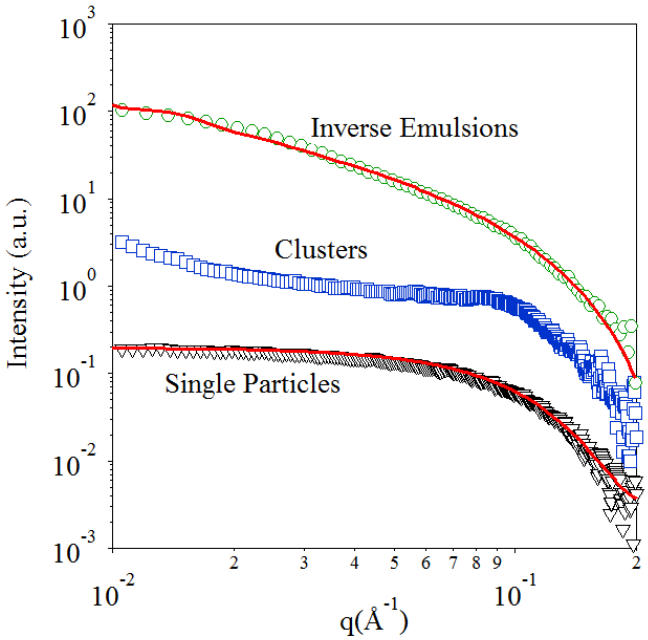


**Figure 3.3.7.** SAXS data of single particles, 0.31PS 20 kDa loaded clusters with MOA, and inverse emulsions with MOA scaled to concentration and then manually shifted for clarity. Solid curves represent data fits to form factor models of a solid sphere and a raspberry-like particle.

SAXS is used to monitor the clustering process. This is an ideal method for studying self-assembly processes because it allows for in-situ, non-destructive monitoring. Additionally, it is a bulk measurement, so the results are averaged over the whole sample population, eliminating unintended bias that is possible with techniques such as TEM. By operating in the dilute regime, structure factor effects can be neglected because the particles are far apart and interparticle correlations are negligible. Figure 3.3.7 shows SAXS curves for single particles, clusters, inverse emulsions, and the respective model fits. As mentioned in the Methods section, the scattering contribution from gold dominates and the contribution from the polymer can be ignored. The single particle curve is fit to the solid sphere model (equation 1) derived by Guinier in 1955 and shown in figure 3.3.7.[44] The fitting is done with SASView and polydispersity is included.[39]

$$I(q) = \frac{vol\ frac}{V}\left[\frac{3V(\Delta\rho)[\sin(qr)-qr\cos(qr)]}{(qr)^3}\right]^2 + background \qquad 3.3.1$$

In equation 1, *vol frac* is the volume fraction of the scattering objects (in this case gold spheres), $V$ is the volume of the scattering object, $r$ is the radius of the sphere, $\Delta\rho$ is the difference is scattering length density between the scattering object and the solvent, and $q$ is the scattering vector. In figure 3.3.7, all curves have the solvent background subtracted. For the sphere fit, the volume fraction and particle size are allowed to vary. The particle size (3.0 nm) matches well with that obtained by TEM (3.0 nm). There is therefore high confidence in the volume fraction ($1.08 \cdot 10^{-5}$ for 0.31PS 20k Da) fit. Additionally, this volume fraction is obtained for each sample before the addition of thiol: $1.11 \cdot 10^{-5}$ for 0.91PS 20 kDa and $1.00 \cdot 10^{-5}$ for 0.25PS 50 kDa. The fitted particle size and volume fraction of bare gold is 3 nm and $3.3 \cdot 10^{-6}$, respectively. Upon clustering, the gold particles are in configurations that allow for repeated correlation lengths, specifically, the distance between particles in a cluster. This length shows up as the peak around 0.1 $Å^{-1}$ in the clustered curve and has been observed in other work of clustered spheres.[15] Additionally, there is an increase in intensity at low q ($0.01 < q < 0.03$ $Å^{-1}$) of the clustered samples compared to the single particles indicating the presence of larger structures. In this case, these structures correspond to larger clusters.

The emulsion curve is fit to a raspberry model developed by Larson-Smith *et al.*[45] Known quantities are fixed to values obtained from other techniques such as DLS, TEM, and SAXS (gold particle size and volume fraction). The entire list of fit parameters and their values is shown in the Appendix. The size of the emulsion is constrained to the smaller population of emulsions (centered around 44 nm in diameter) because that population is the dominant length scale in the q-range of the SAXS experiments. The mean emulsion size obtained from the fit is 64 nm with a lognormal distribution with a polydisperisty ratio (standard deviation/median) of 0.2. The penetration depth of the particle into the emulsion is fixed at zero due to its negligible

effect when the particles are much smaller than the overall emulsion size.[45] For this system, the fractional surface coverage of 0.56 is consistent with literature values for similar nanoparticle surfactants that range from 0.35-0.86.[60]

**3.4 Discussion**

The optical shifts shown in Figure 3.3.1 are due to the coupling of the localized surface plasmon resonance (LSPR) of the particles in the respective assemblies. In order to observe a shift, the particles must be close together, typically within center-to-center distances less than two particle diameters.[61] The requirement of close packing in order to observe significant optical interactions suggests that there is a possible segregation of the small molecules and long polymer chains on the particle surface. The bulky polymer would likely separate the particles by more than two particle diameters center-to-center. Additionally, in the case of the emulsion, the polymer is not soluble in the water phase and thus would have a great preference to be segregated to the outside of the shell. This type of segregation is suggested in a similar system where long chains of poly(ethylene glycol) and short alkane thiols are conjugated to gold particles.[15] Evidence towards their conclusion is based on the increase in optical shift when shorter alkane thiols are used. Since closer interparticle spacing leads to greater optical shifts, they argue that if the polymer is the predominant spacer between particles, the changes in alkane length would not so greatly influence the optical properties of the cluster.

By comparing the peak shift to the increase in absorbance at 800 nm, this suggests that the organization of particles in a shell around the inverse emulsion creates a much larger NIR absorbance coefficient than for clusters of gold particles, which is also consistent with the literature.[62] For spheres of the same diameter, a solid gold particle will have absorbance that is blue shifted compared to an equivalently sized gold shell (i.e. with an optically inactive core).

Furthermore, as the thickness of the shell decreases, the peak will shift to higher wavelengths. This can be used to tune the optical properties of the inverse emulsion by changing the size of the particles that decorate the interface, which effectively act as a gold nanoshell. From SAXS fits, we know that the population of emulsion drops only uses a fraction of the available particles in the dispersion. The remaining particles are free to form clusters as in the absence of water. Therefore, the absorbance curve for the inverse emulsion is an additive result of the different particle configurations in dispersion. Clusters mostly influence absorbance at lower wavelengths and emulsions generally increase the absorbance at higher wavelengths.

The optical effects are explored in more detail in figures 3.3.2 and 3.3.3. In both cases, the shifts remain small until 1 day. Due to the logarithmic scaling of these plots, this suggests that the aggregation is a slow process. This is also supported by the DLS data in figure 4 where again a noticeable increase is first noticed after the 1 day mark. The clustering kinetics are likely affected by the gold concentration. At higher concentrations, collisions between particles and clusters would be more frequent, thus increasing the rate of aggregation. This is exemplified in equation 3.4.1, which shows that the dispersion half-life for diffusion limited aggregation is inversely proportional to the particle number concentration ($n_0$).[34]

$$t_{1/2} = \frac{3\mu}{4kTn_0} \qquad 3.4.1$$

For the particle concentrations used in these experiments, this equation predicts a dispersion half-life of about 9 ms. This suggests aggregation rates that are orders of magnitude faster than those observed in experiments (days). Therefore, reaction-limited aggregation must be taking place due to the steric effects imparted by the polymer.[34]

Figure 3.3.4 shows the change in hydrodynamic diameter over time. The measured hydrodynamic diameter for the bare particles is 4.9 nm, which differs from the actual size, 3.0

nm. This could be due to the low resolution of DLS or due to the contributions of bound molecules (TOAB) that are used to stabilize the bare particles. Additionally, upon addition of the polymer, the hydrodynamic diameter increases. By using the known particle size, the extension of the polymer is estimated to be approximately 5 nm. The upper limit of the polymer extension is set by the theoretical value for a fully extended chain. By using the 2.45 Å monomer length reported by Brûlet et al.[63] this value comes out to 47 nm. Additionally, the lower limit is a fully compressed polymer which is only a few nanometers wide. Neither of these conformations is likely for polystyrene in toluene, so the measured value of 5 nm is consistent with an intermediate degree of extension such as a mushroom conformation.

| Small Molecule | Structure | Stability |
|---|---|---|
| 6-Mercapto-1-hexanol | 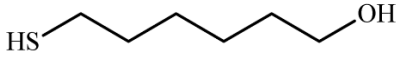  | Least Stable (crashed in 2 days or less) |
| 6-Mercaptohexanoic acid | 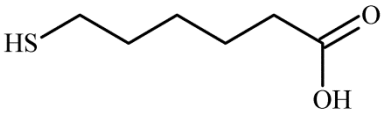  | Intermediately Stable (crashed within 2 months) |
| 8-Mercaptooctanoic acid | 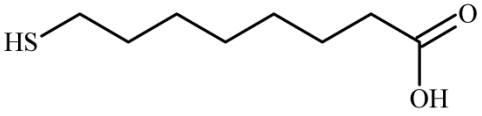  | Most Stable (stable over 2 months) |

**Table 3.4.1.** Cluster stability comparison for three different small molecules used to cluster 0.31PS 20 kDa loaded particles.

In this study, multiple thiolated short molecules (MHO, MHA, MOA) are used in conjunction with different polymer loadings and polymer MW's. A representative summary for a 0.31PS 20 kDa particles clustered with each of the three small molecules is shown in table 3.4.1. For each combination, the dispersions are monitored during short times with DLS and UV-Vis and visually after 1 week. By repeating this for each combination, the following generalizations can be made for the alkyl length and the terminal functionality: 1) for the same alkyl chain length, the alcohol functional groups have a faster rate of clustering than the carboxylic acids and

results in less stable clusters and 2) increasing the chain length by 2 carbon atoms (from 6 to 8) slows the rate of aggregation and also improves the long term stability.

Cluster formation in systems controlling steric repulsion and short range attraction is known to be affected by polymer displacement and by polymer conformation due to changing monolayer density.[35] Shorter alkane thiols have been shown to displace more of the existing thiolated poly(ethylene glycol) from a gold nanoparticle surface than longer ones and denser alkane-thiol monolayers induce a more extended polymer conformation.[35] These two parameters are known to affect the ultimate cluster size.[35] Additionally, it has been shown that shorter mercaptoalkanoic acids pack into more dense monolayers than longer ones on gold nanoparticles.[59] Similar effects related to thiol length could be expected in the system studied here. While both the thiol length and chemistry are varied and likely affect the thiol packing density and polymer conformation, this was not fully quantified in this study.

| Sample | Time to crash |
|---|---|
| 0.31PS 20 kDa | < 4 hrs |
| 0.91PS 20 kDa | < 23 hrs |
| 0.29PS 50 kDa | < 48 hrs |

**Table 3.4.2.** Cluster stability for particles of different polymer surface concentrations and MW's functionalized with 6-Mercapto-1-hexanol.

In addition to effects from the small molecule, the polymer surface concentration and polymer molecular weight also affects the stability as seen in Table 3.4.2. Again, by compiling the data acquired for the different sample sets, the following general trends are observed: 1) for a given MW, a higher loading of polymer increases stability and slows the rate of aggregation and 2) for a given loading, a higher MW increases stability and slows the rate of aggregation. Both of these trends are fairly intuitive, because both polymer MW and polymer surface concentration increase steric repulsion. Higher polymer surface concentrations increase the percentage of

particle surface that is covered and unavailable for particle docking. Meanwhile higher MW chains take up more space than their lower MW counterparts and also reduce the likelihood of particle aggregation. Additionally, the data suggest that MW plays a more significant role than surface concentration based on the results shown in table 3.4.2. Furthermore, TGA also suggests that the larger MW polymer binds much less efficiently than the lower MW. This could be due to poor polymer activity or because the high MW polymer also considerably hinders other polymer chains from binding to the particle surface. This type of behavior is observed in a similar system.[35] Upon subsequent thiol addition, much less high MW polymer is also displaced compared to low MW polymer.

The controlled aggregation of nanoparticle surfactants in non-polar organic solvents is a largely unexplored field. The work presented above provides a versatile platform that opens the door for further exploration into this area. The identification of polymer surface concentration, thiol functionality, and thiol length allows for specific tailoring of cluster properties in future systems. The use of gold demonstrates the viability of this technique for plasmonic applications such as SERS, waveguides, and new metamaterials with negative indices of refraction. Additionally, the use of these particles as nanoparticle surfactants to stabilize water-in-oil emulsions allows for the design of highly stable Pickering emulsions. The Raspberry model can be used to characterize these nanoparticle emulsions, which allows for tuning of specific parameters and intelligent design of these particles.[45] Perhaps most importantly, the work presented here is not limiting. The balance of controlled steric repulsion and short range attraction should be applicable to many systems and is only principally limited by methods for surface conjugation and solvent-polymer compatibility.

### 3.4 Summary and Conclusions

This work demonstrates a method for nanoparticle self-assembly utilizing non-specific interactions in organic solvent. By manipulating the balance of steric repulsion and short range attraction with long polymer chains and small molecules, respectively, it is possible to change the size of particle clusters, their rate of aggregation, and their long term stability. The key parameters include the polymer MW, polymer surface concentration, length of the small molecule, and functionality of the small molecule. The observed trends are similar to those observed for comparable systems in water, which demonstrates the generality of this self-assembly technique. Additionally, these functionalized particles act as amphiphilic nanoparticle surfactants to stabilize the oil-water interface of an inverse emulsion which can be characterized by fitting the SAXS data to a Raspberry model.

## Chapter 4: Nanoparticle Surfactants for Photoacoustic Emulsions

In addition to their uses in cluster formation described previously, amphiphilic nanoparticles have been shown to act as nanoparticle surfactants.[15] They successfully stabilize oil-water interfaces and can therefore be used to stabilize oil-in-water emulsions.[60] Additionally, through use of plasmonic gold particles, an interesting photoacoustic effect is observed that shows promise in theranostic (therapeutic + diagnostic) applications.

### 4.1 Introduction and Background

The photoacoustic (PA) effect is the generation of a sound wave with light. There are several mechanisms for the PA effect as well as several applications which are outlined nicely by Tam.[64] The mechanism of interest for PA emulsions is localized heating around the absorbing particles. In general, this is accomplished through the use of a laser and an absorber within a medium. In this case, gold particles absorb light at a certain wavelength and dissipate that heat to

the surrounding medium. When this heat transfer is sufficiently large, the surrounding medium (liquid) is vaporized, causing a rapid volume change. This expansion generates a pressure wave that is transmitted through the remaining liquid and can be detected by an ultrasound transducer.[65] This is shown schematically in figure 4.1.1.

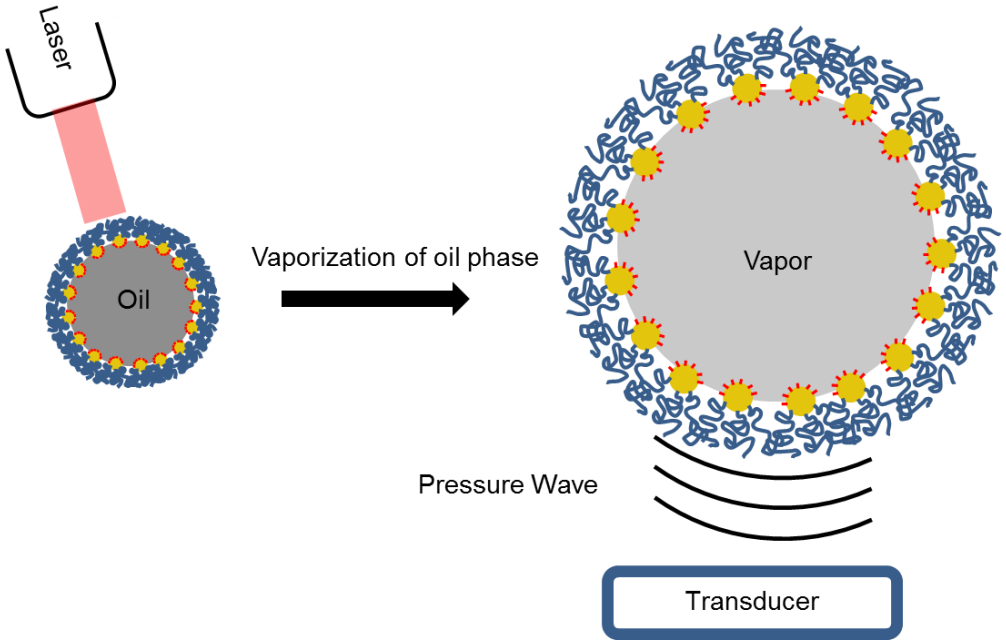


**Figure 4.1.1.** Schematic of emulsion vaporization and sound wave generation.

Due to the potential use of PA effects in medical applications, there is interest in reducing the heat input, thereby avoiding undue heating of surrounding tissue and liquid (blood). There are two main methods to achieve this: reduce the required input laser fluence and reduce the amount of heat required to vaporize the intended liquid. In order to reduce the required input laser fluence, one can attempt to improve the nanoparticle absorbance in the NIR. The NIR corresponds to the "diagnostic window", the wavelength range where human tissue absorbs the least. Thus, a higher percentage of laser light reaches the targeted particles and the tissue it passes through does not heat up as much. Particle decoration is shown to improve the NIR absorbance.[60] To lower the amount of required heat, low boiling point (28°C and 56°C)

fluorinated oils (perfluoropentane and pefluorohexane, respectively) are used. These oils have been successfully used as phase change emulsions for imaging applications and show promise because they limit the heating of the surrounding fluid.[66] One unique benefit of utilizing gold particles to absorb the light is that there is a built in off-switch for heating. The gold particles individually only absorb strongly below about 600 nm. Upon close packing on the surface of an emulsion, the gold shell now absorbs much more strongly in the NIR, which allows for heating. Upon vaporization of the emulsion phase, the particles are spread out on the surface of the newly formed vapor bubble which eliminates LSPR overlap and therefore reduces the absorbance. Therefore, as soon as vaporization is achieved, heating by the laser is stopped.

By combining this PA effect with ultrasound, a combined imaging and therapeutic technique is created that allows for vaporization at low pressures and low laser fluences.[50] By synchronizing laser pulses with the peak negative pressure of an input ultrasound wave, the cavitation probability of the emulsions is increased, which allows for the use of pressures (Mechanical Index < 1.9) and laser fluences (<25 $mJ/cm^2$ at 750 nm) well below safety standards for human use. Minimization of this cavitation threshold is the design goal of these emulsions, which can only be achieved by thorough characterization. The phase change provides contrast for imaging and the pressure wave is shown to break through a blood clot, which is promising for therapeutic applications.[50]

Here we present the initial findings comparing the effects of varying the oil phase as well as the short thiol and their resulting PA/US performance.

## 4.2 Experimental Methods

*Materials*

Gold chloride trihydrate, perfluorohexane (PFH), dithiothreitol (DTT), and sodium citrate are purchased from Sigma Aldrich (St. Louis, MO, USA) and used as received. Perfluoropentane (PFP) is purchased from Fluoromed (Round Rock, TX, USA) and used as received. Thiol alkane terminated poly(ethylene glycol) methyl ether (10 kDa, Mw/Mn = 1.08) (PEG) is purchased from Polymer Source (Dorval (Montreal), Quebec, Canada) and is used as received.

*Nanoparticle Synthesis and Functionalization*

Gold nanoparticles 12 nm in diameter are synthesized following a modified Turkevich method by Frens.[67] As with the Brust synthesis described above, glassware cleanliness is important for ensuring particle monodispersity. Therefore, glassware is soaked overnight in a 2 M KOH in ethanol base bath. This is made by slowly dissolving 120 g of KOH in 120 mL of water (very exothermic!). Subsequently, 1 L of ethanol is slowly added to the solution. Before the synthesis, this soaked glassware is rinsed thoroughly with DI water. In order to make use of the 1 g of $HAuCl_4$, 2.539 mL of DI water is added to the 1 g bottle to make a 1 M solution. Next, 0.5 mL of 1 M gold solution is diluted to 500 mL with DI water to make a 0.001 M gold solution. This solution is brought to a boil with vigorous stirring. Once boiling, 50 mL of 38.8 mM sodium citrate is added at once. Aluminum foil is used to lessen the losses due to water evaporation. After 20 minutes the reaction is complete. The volume fraction is approximately $1 \cdot 10^{-5}$ with variation occurring from losses due to evaporation. To functionalize with PEG, a 5 mM PEG solution is made with 10 kDa PEG. A 150 mM DTT solution is made and is added at a 1:1 molar ratio to the PEG solution to break up any disulfide bonds. The solution is allowed to sit overnight. This PEG solution with DTT is then added to the gold at a nominal loading of 4

chains / $nm^2$ of gold surface area. This is then allowed to sit for 4 days to allow for complete binding. This dispersion is then concentrated using a Millipore Ultrafiltration cell with a 50 kDa filter to approximately 0.7 wt% Au. Although not all of the polymer is expected to bind, it is not thought to affect the emulsion formation, so the time consuming step of dialyzing the sample is not taken for these tests.

*Emulsion Formation*

Functionalized and concentrated gold is diluted to $1.05 \cdot 10^{-6}$ volume fraction Au. For butane thiol, 1 μL of thiol is added to 1 mL of diluted gold and the dispersion is allowed to sit overnight. The next day, 10 μL of PFP of PFH is added and the dispersion is immediately sonicated with a Branson Sonifier with a 1/8 inch tapered tip at 10% amplitude for 30 seconds at a pulse rate of 1 second on, 5 seconds off. Pulsing is used to minimize the temperature increase, which could evaporate the oil phase. For octane and decane thiol, only 15 minutes is allowed to pass between thiol addition and sonication. Pre-chilled DI water was used for dilutions to assist in lowering the temperature in anticipation of the heating upon sonication. For PFP samples, an ice bath was used around the sample to further assist in avoiding oil evaporation. These emulsions are then allowed to sit for 2 days and transported to the photoacoustic lab. Upon arrival, they are allowed to sit still for 20 hours and the supernatant is removed to eliminate larger particles ( > 1 μm). The supernatant is then diluted for different runs. Table 4.2.1 shows the formulations used for each sample.

| Oil | Thiol | Vol. % oil | Vol. % Au | Dilution Factor of Supernatent for Parameter Scan Normalized to 750 nm |
|---|---|---|---|---|
| PFH | Butane | 1 | 1.05E-03 | 9.9 |
| PFH | Octane | 1 | 1.05E-03 | 13.2 |
| PFH | Decane | 1 | 1.05E-03 | 14.2 |
| PFP | Butane | 1 | 1.05E-03 | 5.3 |
| PFP | Octane | 1 | 1.05E-03 | 13.2 |
| PFP | Decane | 1 | 1.05E-03 | 16.5 |

**Table 4.2.1** Formulation information for each emulsion.

*UV-Vis*

Absorbance spectra of the supernatant are collected at approximate volume fractions according to the dilution factors listed in table 4.2.1. They are only approximate because although the settling should only have eliminated a small amount of gold, there is no way of determining what the resulting concentration is. Samples are run in a 1 cm pathlength cell.

*Dynamic Light Scattering (DLS)*

DLS measurements are performed on a Malvern Instruments (Worchestershire, United Kingdom) Zetasizer Nano HT using a 1 cm path length polystyrene cuvette, 633 nm wavelength laser, and correlation times of 10 second correlation times. The concentrations are the same as for UV-Vis.

*Small Angle X-Ray Scattering (SAXS)*

SAXS is performed with an Anton Paar (Graz, Austria) SAXSess equipped with a 1.54 Å CuKα x-ray source. Scattering patterns are collected on image plates that are processed with a PerkinElmer (Waltham, MA) Cyclone Plus. Due to approximately two orders of magnitude difference in scattering length densities of gold (Scattering Length Density (SLD) = $1.25 \cdot 10^{-4}$ Å$^{-2}$) and PEG (SLD = $9.28 \cdot 10^{-6}$ Å$^{-2}$) when compared to water(SLD = $9.47 \cdot 10^{-6}$ Å$^{-2}$), the SAXS data is largely representative of the relative position of nanoparticles within the emulsions

because gold will be the dominant scattering object. The oils (PFH and PFP) have SLD's of 1.37· $10^{-5}$ Å$^{-2}$ and 1.33· $10^{-5}$ Å$^{-2}$, respectively. This provides greater contrast with water than PEG, but is still much less than with gold. The emulsions are run at the same concentration as UV-Vis. Scattered x-rays are collected on an image plate that is analyzed with the OptiQuant (PerkinElmer) software. Subsequent data reduction is performed in SAXSQuant 2D (Anton Paar) and SAXSQuant 3.70 (Anton Paar). The data reduction procedure accounts for background contributions from the cell and solvent. Data is put into absolute scale by measuring water as a standard and using the known scattering cross section of water (0.01641 cm$^{-1}$). Fits are performed using the data analysis software SASView with smeared models.[39]

*Parameter Scan*

The parameter scan is performed using the setup described elsewhere.[68]

**4.3 Results**

Figure 4.3.1 shows absorbance curves for PFP samples that are diluted to have the same absorbance at 750 nm. Figure 4.3.2 shows normalized curves for PFH samples. In both samples, butane provides the most intense peak around 520 nm, corresponding to single particles, while octane and decane samples show more broadening of absorbance at higher wavelengths.

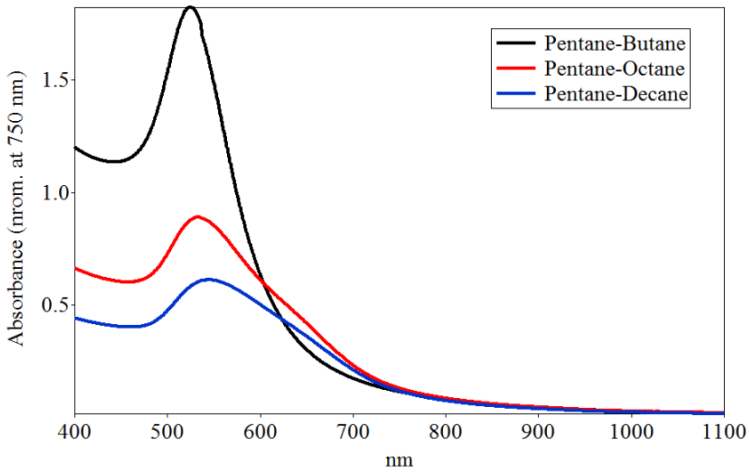


**Figure 4.3.1** Absorbance curves of PFP samples normalized to absorbance at 750 nm.

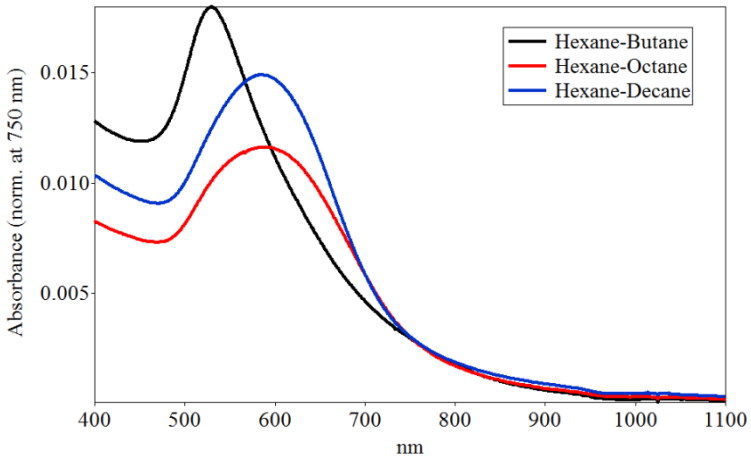


**Figure 4.3.2** Absorbance curves of PFH samples normalized to absorbance at 750 nm.

Figure 4.3.3 shows volume distributions obtained from the DLS for PFP samples and figure 4.3.4 shows the same for PFH samples.

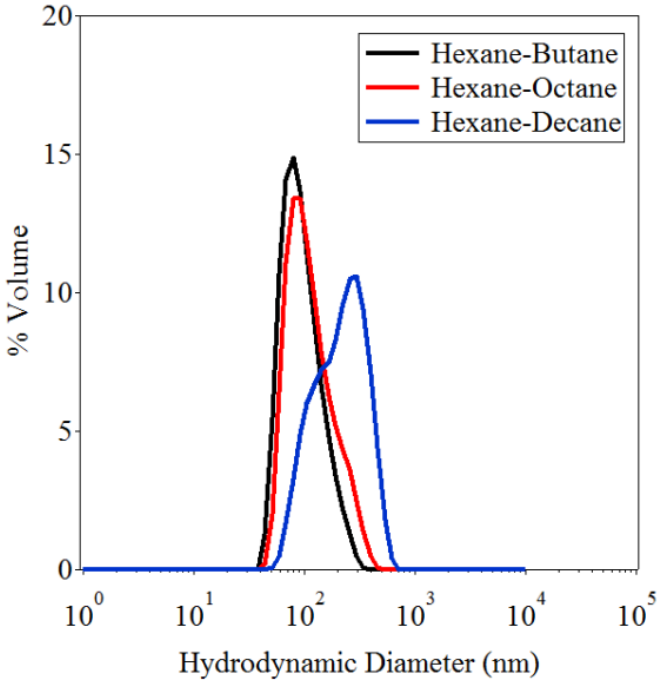


**Figure 4.3.3** Volume distribution of PFH emulsions.

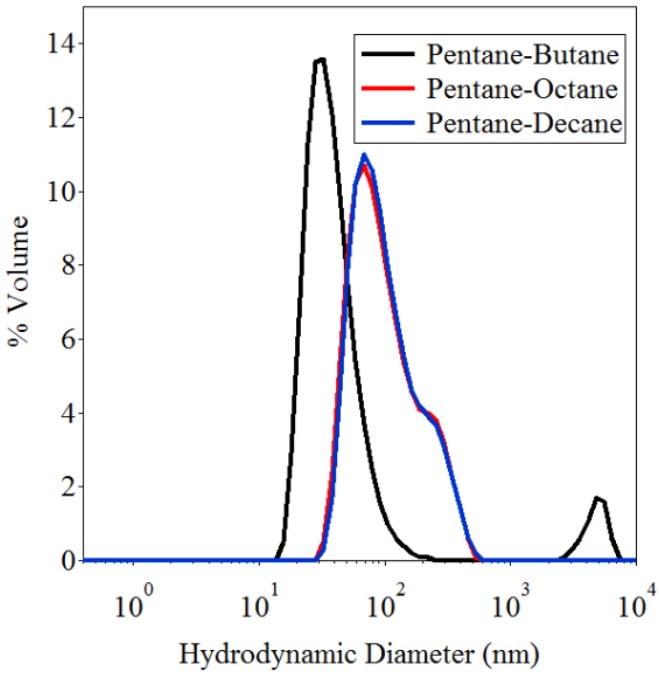


**Figure 4.3.4** Volume distribution of PFP emulsions.

Figure 4.3.5 shows a cavitation probability curve for a PFH emulsion with decane thiol. The laser fluence is varied and it is clear that the cavitation threshold decreases with increasing laser fluence.

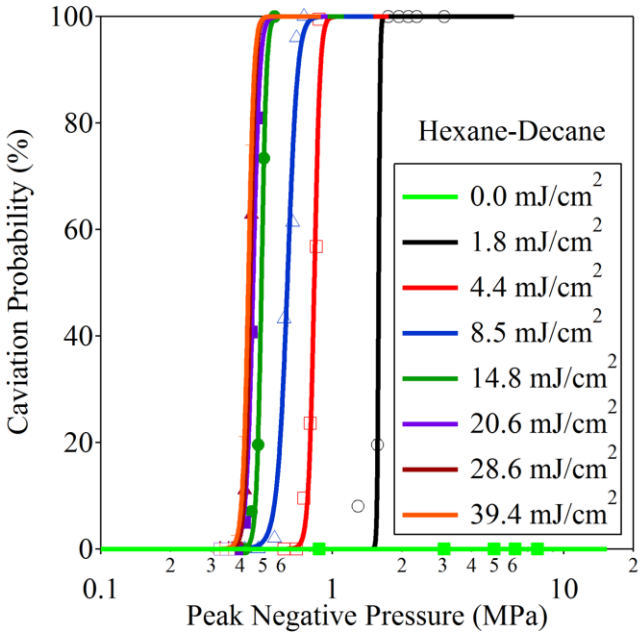


**Figure 4.3.5** Cavitation probability as a function of peak negative pressure at different laser fluences for PFH emulsions with mercaptodecane.

Figure 4.3.6 shows a comparison of cavitation probability for each sample at constant laser fluence. There are clear differences in performance for the PFP samples with octane thiol providing the lowest threshold. Less obvious differences are seen for the PFH samples, but octane thiol again requires the lowest threshold pressure.

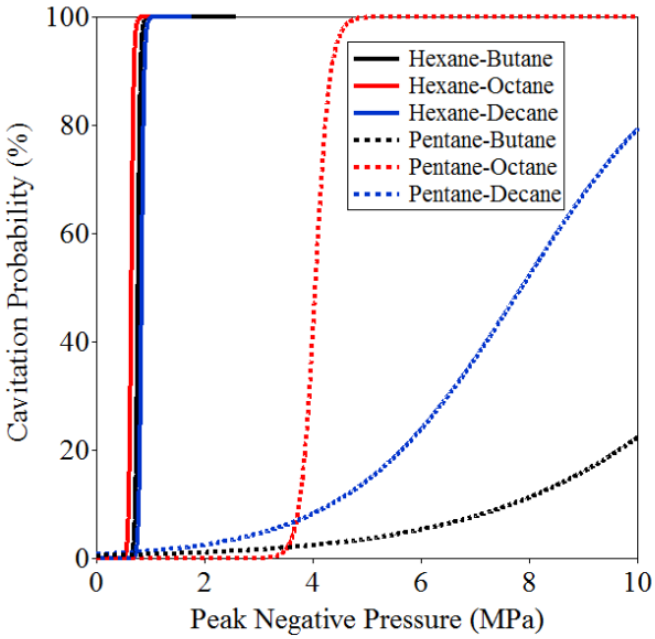


**Figure 4.3.6** Cavitation probability at 4.4 mJ/ $cm^2$ for different emulsions as a function of peak negative pressure.

Figure 4.3.7 shows a combination plot of laser fluence and peak negative pressure as well as the safety limits. The maximum laser fluence allowed for human diagnostics at 750 nm is 25 $mJ/cm^2$ and the maximum mechanical index (MI) is 1.9, which relates to the power of the ultrasound. Several PFH samples fall within the acceptable range (left of MI line and below fluence line) while PFP samples are much closer to the threshold and many fall outside of these limits. The laser fluence and peak negative pressure reported is determined by using the 50% cavitation probability. Figures 4.3.5 and 4.3.6 are sample curves and each was generated for every combination presented in table 4.2.1.

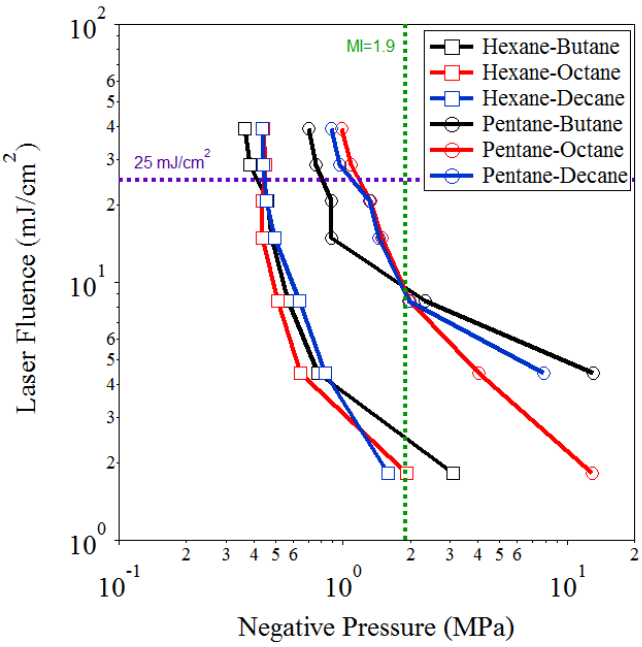


**Figure 4.3.7** Parameter map of different emulsions corresponding to 50% cavitation probability as well as safety limits (dotted lines).

### 4.4 Discussion

In order to make structure function relationships, it is important to first determine the best performing emulsions. Figure 4.3.7 suggests that PFH with octane thiol is the best performer because it shows cavitation at the lowest laser fluence and peak negative pressure. However, due to the accuracy of the parameter scan, all PFH samples perform roughly the same and collectively better than the PFP samples. In fact, the PFP samples behave similarly to pure gold with no oil as seen in work by Arnal et al.[68] This is interesting, because it suggests something about the presence of oil in the emulsions. As PFP is the lower boiling point oil, it is possible that some evaporated, resulting in smaller emulsions as seen in comparison of figures 4.3.3 and 4.3.4. Another possibility is that the amphiphilic particles form swollen clusters with the addition of oil instead of emulsion droplets decorated with particles. In any case, it is interesting that the lower boiling point oil performs more poorly than the higher boiling point oil. Further study is needed to explore this behavior.

Figures 4.3.3 and 4.3.4 show that butane thiol reliably makes the smallest emulsions while decane thiol makes the largest. It has been shown that thiol length changes the polymer conformation, which can change the steric repulsion around the particle.[35] In that work, an optimal alkane thiol length is found to be 8 carbons long. It is reasoned that there is interplay between the monolayer packing density and the replacement of polymer by the thiol, which together determines this optimum. Shorter thiols are shown to replace more polymer, while longer thiols form more dense monolayers. Removing more polymer decreases the amount of steric repulsion to surrounding particles, while a tighter monolayer forces a more extended polymer conformation, again allowing for better access for incoming particles. Because the system used in this work is nearly identical to that by Larson-Smith et al. it is extremely likely that the same effects occur for self-assembly at the interface of an O/W emulsion. With increased steric repulsion, particles are forced farther apart, thus decreasing the packing density. Packing density is shown to affect the plasmonic properties of particle clusters.[69] Increasing the interparticle spacing decreases the degree of plasmon coupling and would thus reduce the absorbance at higher wavelengths. This is useful for design of these emulsions, because it is clear that higher packing density would help improve the absorption characteristics of the emulsion. Another effect demonstrated by Larson-Smith et al. is that the length of the alkane thiol can also influence the optical properties of self-assembled gold particles.[35] Shorter thiols cause greater optical shifts, which is consistent with decreasing the interparticle spacing for a greater degree of plasmon coupling. Due to the effects discussed above, it is logical that an intermediate thiol length is desired for optimal performance. In this study, only 3 alkane lengths were studied, but the intermediate length (octane thiol) does appear to produce the best performing emulsions.

Figure 4.3.1 and 4.3.2 show the absorbance spectra for both PFH and PFP emulsions. Because the performance of the emulsions is largely due to the optical properties, it would follow that the UV-Vis data provide insights into predicting the best performer. Table 4.2.1 shows that the dilution factor increases with the length of the thiol. This would suggest that decane thiol produces the most efficient emulsions. However, as seen by the cavitation data, octane thiol seems to perform the best. This apparent discrepancy is not easily explained and further characterization is needed to isolate the effects of each parameter (see section 5.2).

### 4.5 Summary and Conclusions

This work demonstrates the viability of nanoparticle-stabilized, fluorinated O/W emulsions for PA/US theranostics. It is shown that PFH emulsions perform better than PFP emulsions and that alkane thiol lengths of 8 or 10 carbons perform better than 4 carbon chains. PFH emulsions can be cavitated below human safety standards of both laser fluence and ultrasound pressure, which indicates their promise in theranostic applications.

## Chapter 5: Future Work

The following chapter describes preliminary data as well as a discussion of what experiments might naturally follow the results presented in the previous chapters.

### 5.1 Nanoparticle Self-Assembly

The work presented in Chapter 3 describes a new method for controlling self-assembly of nanoparticle surfactants in non-polar organic solvents. This work successfully demonstrates the ability to control self-assembly by varying the polymer surface concentration, the polymer MW, and the short thiol length and chemistry. Trends were qualitatively obtained for these parameters, but a more in depth study is needed to quantify them. The interesting parameters to quantify are the surface concentration of polymer and thiol and how they are affected by MW, length, and

functionality. These experiments would involve more detailed TGA studies or potentially utilized neutron scattering. Neutron scattering can also be used to obtain the polymer conformation in these systems. Preliminary data has been taken for this purpose and is shown in figure 5.1.1.

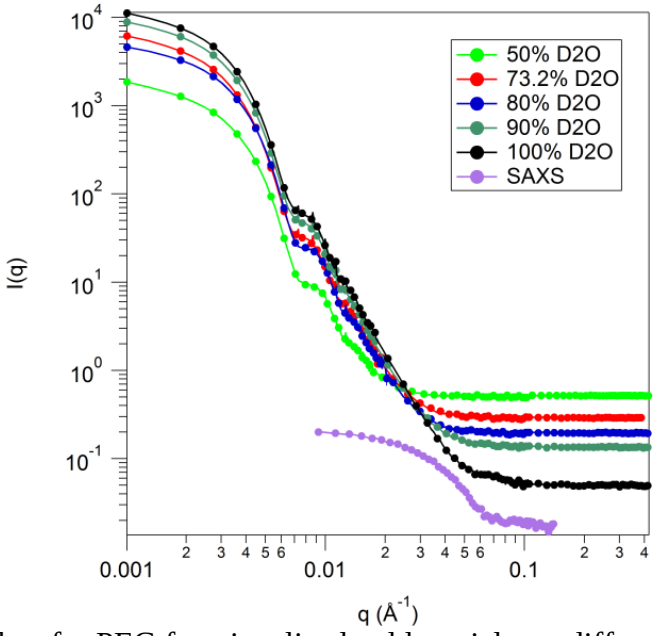


**Figure 5.1.1** SANS data for PEG functionalized gold particles at different contrasts as well as SAXS data.

In this experiment, contrast variation was used in order to obtain neutron scattering curves at 5 different solvent deuteration levels. This is done in order to gain confidence in the fitting since scattering curves are not unique. By simultaneously fitting these curves, one can obtain the polymer conformation. The choice of model, however, is more challenging. Figure 5.1.2 shows a simultaneous fit to a Core-Shell model in Igor. It is clear that although the Core-Shell model fits the curves generally, it does not match exactly. This is likely due to the over simplification of the polymer as a pure shell of constant density, when it is known to change in density with the distance from the surface.[42]

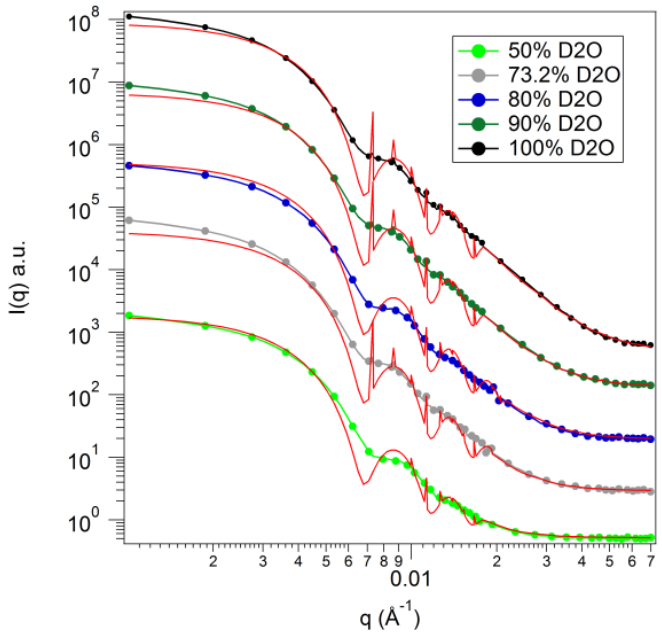


**Figure 5.1.2** SANS data of PEG functionalized gold particles at different contrasts with core-shell simultaneous fits (red lines).

In order to more accurately fit these data, a more detailed model is required. Such a model has been developed by the Cosgrove group and has been shown to be extremely accurate for polymer brushes that are small relative to the particle size.[43] For the nanoparticles used in this work, the polymer extension is of the same order of magnitude as the particle size, so the simplified equations used by Cosgrove et al. are not valid. These equations found in reference 40 need to be derived for the general case. This would be useful for determining the change in polymer conformation upon addition of thiol. Once the model is developed for single particles, it can then be used to analyze clustered systems. This would extremely valuable, because it could determine where the polymer resides in clustered sample and could shed light onto what these structures look like in dispersion

Another area of future work in the self-assembly of nanoparticles is to expand to different interparticle forces to induce clustering. One of these forces is electrostatic attraction. Electrostatics provide powerful attractive and repulsive forces that could be utilized to create

strongly formed self-assembled structures. Additionally, charges can be imparted by several functional groups (carboxylic acid, alcohol, amine, etc.). By combining a population of positively charged particles with a population of negatively charged particles, aggregation is induced. Figure 5.1.3 shows the zeta potential curves for two populations of particles, one functionalized with an anionic thiol and one with a cationic thiol.

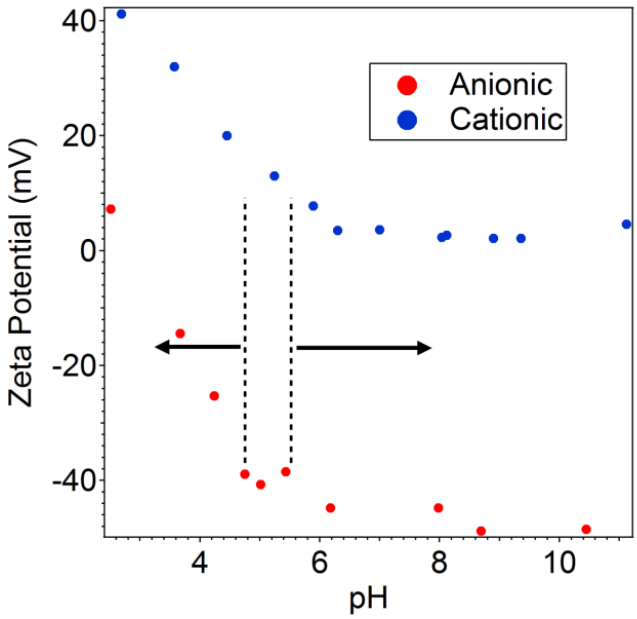


**Figure 5.1.3** Zeta-potentials as a function of pH of thiol functionalized gold (red - mercaptooctanoic acid, blue – (11-mercaptoundecyl) trimethyl ammonium bromide)

When the functional groups reach their pKa, they change their protonation state and therefore either gain or lose charge. With the thiols used here, there is only a small pH range where both thiols are charged. The ideal choice of thiols would be ones who possess a high surface charge (>|20| mV) over a wide overlapping pH range, or at least the range of interest for their application. An additional benefit of pH dependent charging is the ability to turn the attraction on and off by manipulating the pH of the dispersion. This could have potential benefits for breaking apart the aggregates or selectively inducing clustering. Additionally, it is shown that steric stabilization by grafted PEG chains does inhibit aggregation when the particles lose their

surface charge as shown in Figure 5.1.4. Therefore, steric repulsion can be used to counteract electrostatic attraction and the balance between the two should allow for controlled self-assembly.

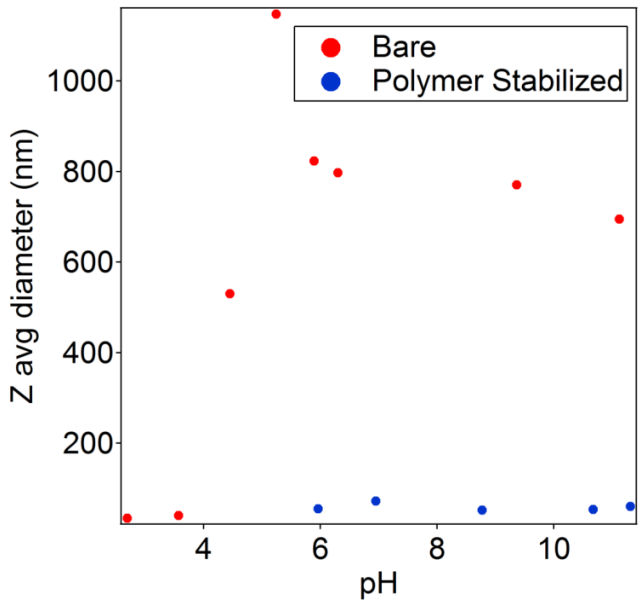


**Figure 5.1.4** Z-average diameter as a function of pH of acid functionalized particles with and without polymer.

In addition to the two projects briefly described in this section, longer term goals for the self-assembly of nanoparticle surfactants include more complex geometries and multi-component aggregates. This could include clustering different shapes such as rods or cubes and clustering particles of different composition, such as a combined silver/gold clusters. Silver/gold clusters are interesting for organic photovoltaics where combination of these two types of particles has been shown to achieve a maximum performance enhancement compared to pure particle populations.[70]

**5.2 Photoacoustic Emulsions**

For the photoacoustic emulsion work described in Chapter 4, more detailed characterization is needed in order to enable direct structure-property relationships. Fitting with the Raspberry model as done for the emulsions in Chapter 3 should also be possible for the O/W

emulsions used for photoacoustic/ultrasound theranostics. In order to obtain meaningful values from the fit, a higher degree of front end characterization is needed. Due to the complimentary effects of emulsion volume fraction and surface coverage, it is possible to obtain similar fits by changing both parameters. Thus, because the surface coverage is not obtainable via other techniques, it is critical to accurately measure the emulsion volume fraction. Another valuable parameter is the number concentration of emulsions. This is needed for the most accurate scaling of the absorbance data because it allows one to determine performance based on particle efficiency instead of absolute population performance. This might be achievable by some sort of flow cytometer like system, where only one particle at a time is allowed to pass through an orifice at one time. Additionally, characterization of individual emulsions would allow for the most direct comparison of synthesis and performance by eliminating the population averaging effects. To better understand the structure of the emulsions, cyro-electron microscopy (Cryo-EM) could be used to visualize the emulsions as they are in dispersion. This could be used to obtain an approximate surface coverage and also determine the particle organization on the surface (i.e. patches, loose or tight packing, etc.).

Ultimately, the structure-function relationships are needed for intelligent design of these emulsions. Finding the optimal formulation will be critical in accelerating these particles into animal studies, which will ultimately show their true behavior and feasibility.

**Chapter 6: Summary**

The work presented in this thesis centers on the self-assembly of nanoparticle surfactants. Gold nanoparticles are rendered amphiphilic by grafting long polymer chains and small thiolated molecules having opposite hydrophobicity. This is done in both organic solvent to form clusters and in water to form O/W emulsions with fluorinated oils. Both systems utilize a balance of

steric repulsion and short range attraction to control self-assembly. Clustering in non-polar organic solvents is shown to depend on the polymer MW, polymer surface concentration, length of the small molecule, and functionality of the small molecule. These parameters control the size and stability of the aggregates. For O/W emulsions, the fluorinated oil and the alkane thiol length are shown to affect the size and optical properties of the emulsions. This work provides a platform for nanoparticle self-assembly which can be tuned to other systems of different particles and solvents.

**Appendix:**

| | |
|---|---|
| Volume Fraction of Emulsion | 0.0046 |
| Radius of Emulsion (Å) | 319 |
| Polydispersity of Emlusion | 0.20 |
| SLD Emulsion ($Å^{-2}$) | 9.47E-06 |
| Volume Fraction of Gold Particles | 3.31E-05 |
| Radius of Gold Particles (Å) | 15 |
| Fractional Surface Coverage | 0.43 |
| SLD of Gold Particles ($Å^{-2}$) | 0.000125 |
| Penetration | 0 |
| SLD Solvent ($Å^{-2}$) | 8.03E-06 |
| Background ($cm^{-1}$) | 0 |

**Table A1**. Values obtained from fit to raspberry model.

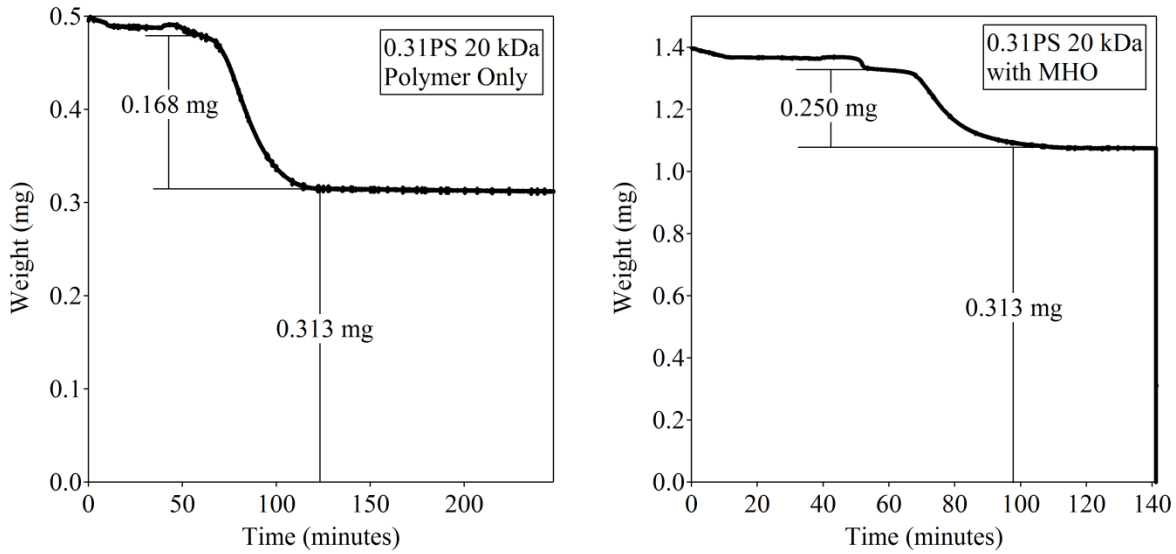


**Figure A1**. TGA curves for 0.31PS 20 kDa sample polymer only (left) and after addition of MOA (right).

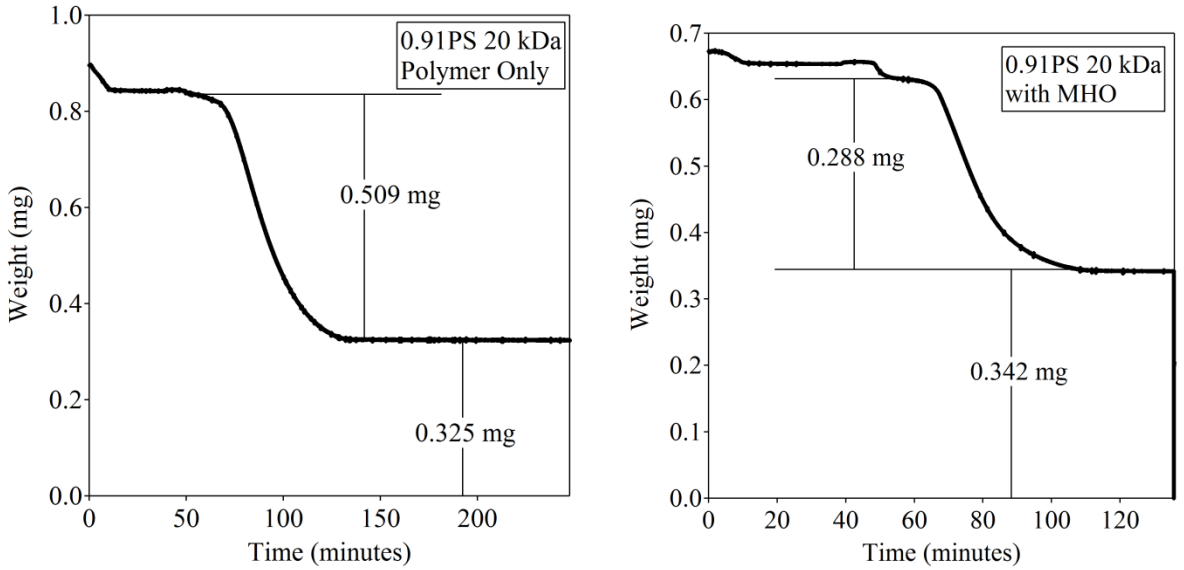


**Figure A2**. TGA curves for 0.91PS 20 kDa sample polymer only (left) and after addition of MOA (right).

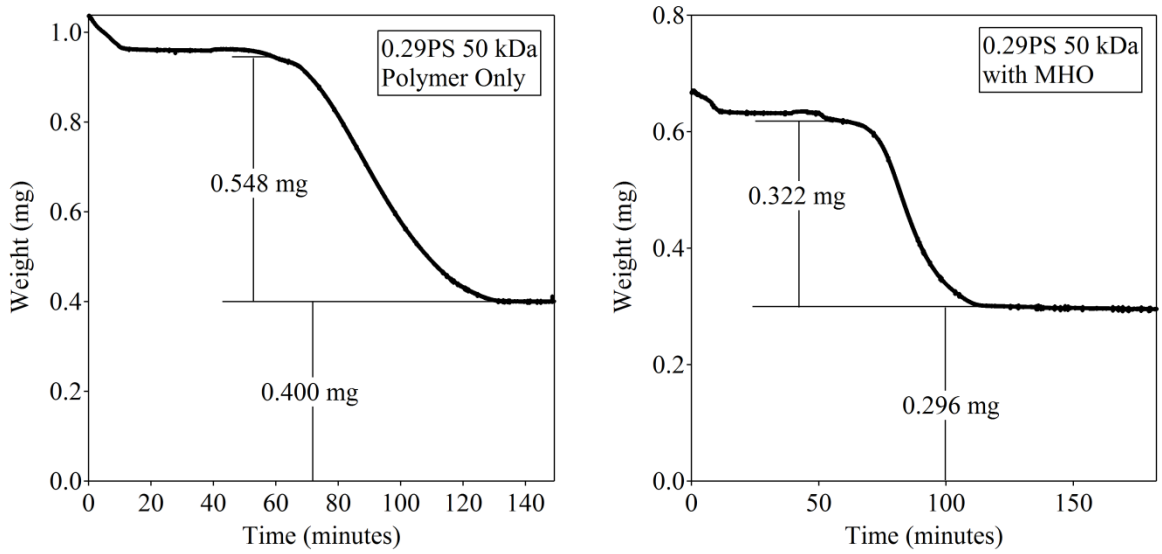


**Figure A3**. TGA curves for 0.29PS 50 kDa sample polymer only (left) and after addition of MOA (right).

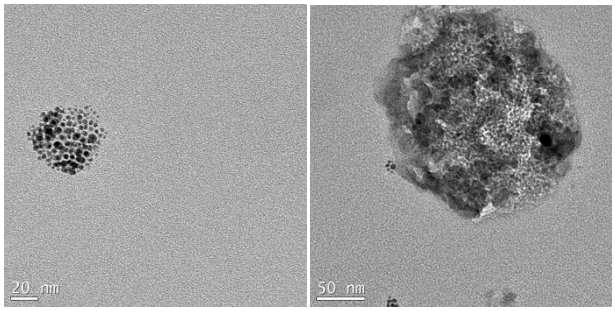


**Figure A4**. TEM images of frozen emulsion samples.

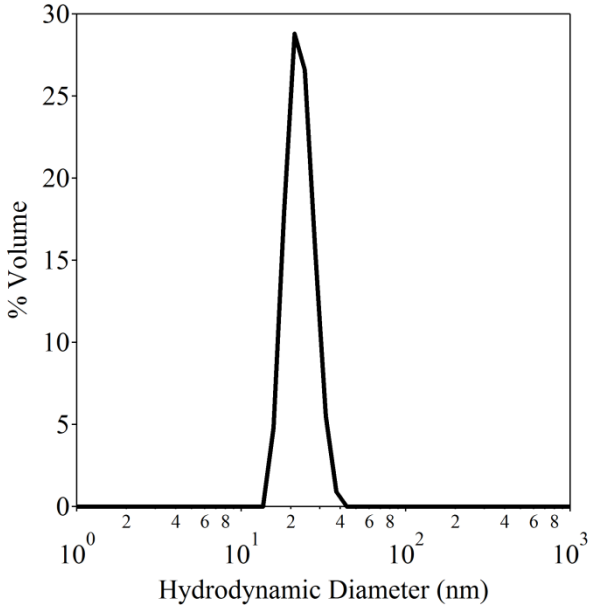


**Figure A 5**. DLS volume distribution of sonicated clusters.

References


(1) Whitesides, G. M.; Grzybowski, B. Self-Assembly at All Scales. *Science* **2002**, *295*, 2418–2421.

(2) Bishop, K. J. M.; Wilmer, C. E.; Soh, S.; Grzybowski, B. a. Nanoscale Forces and Their Uses in Self-Assembly. *Small* **2009**, *5*, 1600–1630.

(3) Qiao, R.; Yang, C.; Gao, M. Superparamagnetic Iron Oxide Nanoparticles: From Preparations to in Vivo MRI Applications. *J. Mater. Chem.* **2009**, *19*, 6274.

(4) Kim, K.; Carroll, D. L. Roles of Au and Ag Nanoparticles in Efficiency Enhancement of poly(3-octylthiophene)/C[sub 60] Bulk Heterojunction Photovoltaic Devices. *Appl. Phys. Lett.* **2005**, *87*, 203113.

(5) Gehan, H.; Fillaud, L.; Chehimi, M. M.; Aubard, J.; Hohenau, A.; Felidj, N. Thermo-Induced Electromagnetic Coupling in Gold / Polymer Hybrid Plasmonic Structures Probed by Surface-. **2010**, *4*, 6491–6500.

(6) Urzhumov, Y. a; Shvets, G.; Fan, J. a; Capasso, F.; Brandl, D.; Nordlander, P. Plasmonic Nanoclusters: A Path towards Negative-Index Metafluids. *Opt. Express* **2007**, *15*, 14129–14145.

(7) Alegret, J.; Rindzevicius, T.; Pakizeh, T.; Alaverdyan, Y.; Gunnarsson, L.; Käll, M. Plasmonic Properties of Silver Trimers with Trigonal Symmetry Fabricated by Electron-Beam Lithography. *J. Phys. Chem. C* **2008**, *112*, 14313–14317.

(8) Thomas, K. G.; Barazzouk, S.; Ipe, B. I.; Joseph, S. T. S.; Kamat, P. V. Uniaxial Plasmon Coupling through Longitudinal Self-Assembly of Gold Nanorods. *J. Phys. Chem. B* **2004**, *108*, 13066–13068.

(9) Liao, J. H.; Chen, K. J.; Xu, L. N.; Ge, C. W.; Wang, J.; Huang, L.; Gu, N. Self-Assembly of Length-Tunable Gold Nanoparticle Chains in Organic Solvents. *Appl. Phys. A Mater. Sci. Process.* **2003**, *76*, 541–543.

(10) Yap, F. L.; Thoniyot, P.; Krishnan, S.; Krishnamoorthy, S. Nanoparticle Cluster Arrays for High-Performance SERS through Directed Self-Assembly on Flat Substrates and on Optical Fibers. *ACS Nano* **2012**, *6*, 2056–2070.

(11) Lu, Z.; Yin, Y. Colloidal Nanoparticle Clusters: Functional Materials by Design. *Chem. Soc. Rev.* **2012**, *41*, 6874–6887.

(12) Aldaye, F. a; Sleiman, H. F. Dynamic DNA Templates for Discrete Gold Nanoparticle Assemblies: Control of Geometry, Modularity, Write/erase and Structural Switching. *J. Am. Chem. Soc.* **2007**, *129*, 4130–4131.

(13) Paquet, C.; Pagé, L.; Kell, A.; Simard, B. Nanobeads Highly Loaded with Superparamagnetic Nanoparticles Prepared by Emulsification and Seeded-Emulsion Polymerization. *Langmuir* **2010**, *26*, 5388–5396.

(14) Urban, A. S.; Shen, X.; Wang, Y.; Large, N.; Wang, H.; Knight, M. W.; Nordlander, P.; Chen, H.; Halas, N. J. Three-Dimensional Plasmonic Nanoclusters. *Nano Lett.* **2013**, *13*, 4399–4403.

(15) Larson-Smith, K.; Pozzo, D. C. Scalable Synthesis of Self-Assembling Nanoparticle Clusters Based on Controlled Steric Interactions. *Soft Matter* **2011**, *7*, 5339.

(16) Sánchez-Iglesias, A.; Grzelczak, M.; Altantzis, T.; Goris, B.; Pérez-Juste, J.; Bals, S.; Van Tendeloo, G.; Donaldson, S. H.; Chmelka, B. F.; Israelachvili, J. N.; et al. Hydrophobic Interactions Modulate Self-Assembly of Nanoparticles. *ACS Nano* **2012**, *6*, 11059–11065.

(17) Morfa, A. J.; Rowlen, K. L.; Reilly, T. H.; Romero, M. J.; van de Lagemaat, J. Plasmon-Enhanced Solar Energy Conversion in Organic Bulk Heterojunction Photovoltaics. *Appl. Phys. Lett.* **2008**, *92*, 013504.

(18) Hentschel, M.; Schäferling, M.; Weiss, T.; Liu, N.; Giessen, H. Three-Dimensional Chiral Plasmonic Oligomers. *Nano Lett.* **2012**, *12*, 2542–2547.

(19) Sanguansri, P.; Augustin, M. A. Nanoscale Materials Development – a Food Industry Perspective. *Trends Food Sci. Technol.* **2006**, *17*, 547–556.

(20) Krawczyk, M. A.; Wasan, D. T.; Shetty, C. S. Chemical Demulsification of Petroleum Emulsions Using Oil-Soluble Demulsi F Ier S. **1991**, 367–375.

(21) Frelichowska, J.; Bolzinger, M.-A.; Pelletier, J.; Valour, J.-P.; Chevalier, Y. Topical Delivery of Lipophilic Drugs from O/w Pickering Emulsions. *Int. J. Pharm.* **2009**, *371*, 56–63.

(22) Pickering, S. Emulsions. *J. Chem. Soc. Faraday Trans.* **1907**, *91*, 2001–2021.

(23) Tu, F.; Park, B. J.; Lee, D. Thermodynamically Stable Emulsions Using Janus Dumbbells as Colloid Surfactants. *Langmuir* **2013**, *29*, 12679–12687.

(24) Chen, T.; Colver, P. J.; Bon, S. a. F. Organic–Inorganic Hybrid Hollow Spheres Prepared from TiO2-Stabilized Pickering Emulsion Polymerization. *Adv. Mater.* **2007**, *19*, 2286–2289.

(25) Kumar, A.; Park, B. J.; Tu, F.; Lee, D. Amphiphilic Janus Particles at Fluid Interfaces. *Soft Matter* **2013**, *9*, 6604.

(26) Glaser, N.; Adams, D. J.; Bo, A.; Krausch, G. Janus Particles at Liquid - Liquid Interfaces. **2006**, 5227–5229.

(27) Mason, T. G.; Wilking, J. N.; Meleson, K.; Chang, C. B.; Graves, S. M. Nanoemulsions: Formation, Structure, and Physical Properties. *J. Phys. Condens. Matter* **2006**, *18*, R635–R666.

(28) Solans, C.; Izquierdo, P.; Nolla, J.; Azemar, N.; Garciacelma, M. Nano-Emulsions. *Curr. Opin. Colloid Interface Sci.* **2005**, *10*, 102–110.

(29) Taylor, P. Ostwald Ripening in Emulsions: Estimation of Solution Thermodynamics of the Disperse Phase. *Adv. Colloid Interface Sci.* **2003**, *106*, 261–285.

(30) Kleinman, S. L.; Sharma, B.; Blaber, M. G.; Henry, A.; Valley, N.; Gri, R.; Natan, M. J.; Schatz, G. C.; Duyne, R. P. Van. Structure Enhancement Factor Relationships in Single Gold Nanoantennas by Surface-Enhanced Raman Excitation Spectroscopy. **2013**.

(31) Maier, S. a; Kik, P. G.; Atwater, H. a; Meltzer, S.; Harel, E.; Koel, B. E.; Requicha, A. a G. Local Detection of Electromagnetic Energy Transport below the Diffraction Limit in Metal Nanoparticle Plasmon Waveguides. *Nat. Mater.* **2003**, *2*, 229–232.

(32) Jain, P. K.; Lee, K. S.; El-Sayed, I. H.; El-Sayed, M. a. Calculated Absorption and Scattering Properties of Gold Nanoparticles of Different Size, Shape, and Composition: Applications in Biological Imaging and Biomedicine. *J. Phys. Chem. B* **2006**, *110*, 7238–7248.

(33) Link, S.; Mohamed, M. B.; El-Sayed, M. a. Simulation of the Optical Absorption Spectra of Gold Nanorods as a Function of Their Aspect Ratio and the Effect of the Medium Dielectric Constant. *J. Phys. Chem. B* **1999**, *103*, 3073–3077.

(34) Berg, J. *An Introduction to Interfaces & Colloids: The Bridge to Nanoscience*; World Scientific Publishing Co.Pte. Ltd.: Singapore, 2010; pp. 562–565.

(35) Larson-Smith, K.; Pozzo, D. C. Competitive Adsorption of Thiolated Poly(ethylene Glycol) and Alkane-Thiols on Gold Nanoparticles and Its Effect on Cluster Formation. *Langmuir* **2012**, *28*, 13157–13165.

(36) Pielichowski, K.; Flejtuch, K. Non-Oxidative Thermal Degradation of Poly(ethylene Oxide): Kinetic and Thermoanalytical Study. *J. Anal. Appl. Pyrolysis* **2005**, *73*, 131–138.

(37) Hammouda, B. Probing Nanoscale Structures - The SANS Toolbox.

(38) Lindner, P.; Zemb, T. *Nuetrons, X-Rays and Light: Scattering Methods Applied to Soft Condensed Matter*; First.; Elsevier Science B.V.: Amsterdam, The Netherlands, 2002.

(39) SASView.www.sasview.org.

(40) Cosgrove, T. Volume-Fraction Profiles of Adsorbed Polymers. *J. Chem. Soc. Faraday Trans.* **1990**, *86*, 1323.

(41) Cosgrove, T.; Hone, J. H. E. A Small-Angle Neutron Scattering Study of the Structure of Gelatin at the Surface of Polystyrene Latex Particles. **1998**, *7463*, 5376–5382.

(42) Hone, J. H. E.; Cosgrove, T.; Saphiannikova, M.; Obey, T. M.; Marshall, J. C.; Crowley, T. L. Structure of Physically Adsorbed Polymer Layers Contrast Variation Methods. **2002**, 855–864.

(43) Marshall, J. C.; Cosgrove, T.; Leermakers, F.; Obey, T. M. Detailed Modeling of the Volume Fraction Profile of Adsorbed Polymer Layers Using Small-Angle Neutron Scattering. **2004**, 4480–4488.

(44) Guinier, A. *Small-Angle Scattering of X-Rays*; John Wiley & Sons, Inc.: New York, 1955.

(45) Larson-Smith, K.; Jackson, A.; Pozzo, D. C. Small Angle Scattering Model for Pickering Emulsions and Raspberry Particles. *J. Colloid Interface Sci.* **2010**, *343*, 36–41.

(46) Zharov, V. P.; Mercer, K. E.; Galitovskaya, E. N.; Smeltzer, M. S. Photothermal Nanotherapeutics and Nanodiagnostics for Selective Killing of Bacteria Targeted with Gold Nanoparticles. *Biophys. J.* **2006**, *90*, 619–627.

(47) Lu, Z.; Duan, J.; He, L.; Hu, Y.; Yin, Y. Mesoporous TiO 2 Nanocrystal Clusters for Selective Enrichment of Phosphopeptides. **2010**, *82*, 7249–7258.

(48) Qiu, P.; Jensen, C.; Charity, N.; Towner, R.; Mao, C. Oil Phase Evaporation-Induced Self-Assembly of Hydrophobic Nanoparticles into Spherical Clusters with Controlled Surface Chemistry in an Oil-in-Water Dispersion and Comparison of Behaviors of Individual and Clustered Iron Oxide Nanoparticles. *J. Am. Chem. Soc.* **2010**, *132*, 17724–17732.

(49) Wei, C.-W.; Lombardo, M.; Larson-Smith, K.; Pelivanov, I.; Perez, C.; Xia, J.; Matula, T.; Pozzo, D.; O'Donnell, M. Nonlinear Contrast Enhancement in Photoacoustic Molecular Imaging with Gold Nanosphere Encapsulated Nanoemulsions. *Appl. Phys. Lett.* **2014**, *104*, 033701.

(50) Wei, C.; Xia, J.; Lombardo, M.; Perez, C.; Arnal, B.; Larson-Smith, K.; Pelivanov, I.; Matula, T.; Pozzo, L.; O'Donnell, M. Laser-Induced Cavitation in Nanoemulsion with Gold Nanospheres for Blood Clot Disruption: In Vitro Results. *Opt. Lett.* **2014**, *39*, 2599–2602.

(51) Gan, Q.; Bartoli, F. J.; Kafafi, Z. H. Plasmonic-Enhanced Organic Photovoltaics: Breaking the 10% Efficiency Barrier. *Adv. Mater.* **2013**, *25*, 2385–2396.

(52) Kozanoglu, D.; Apaydin, D. H.; Cirpan, A.; Esenturk, E. N. Power Conversion Efficiency Enhancement of Organic Solar Cells by Addition of Gold Nanostars, Nanorods, and Nanospheres. *Org. Electron.* **2013**, *14*, 1720–1727.

(53) Chen, X.; Yang, X.; Fu, W.; Xu, M.; Chen, H. Enhanced Performance of Polymer Solar Cells with a Monolayer of Assembled Gold Nanoparticle Films Fabricated by Langmuir–Blodgett Technique. *Mater. Sci. Eng. B* **2013**, *178*, 53–59.

(54) Han, X.; Goebl, J.; Lu, Z.; Yin, Y. Role of Salt in the Spontaneous Assembly of Charged Gold Nanoparticles in Ethanol. *Langmuir* **2011**, *27*, 5282–5289.

(55) Taratula, O.; Chen, A. M.; Zhang, J.; Chaudry, J.; Nagahara, L.; Banerjee, I.; He, H. Highly Aligned Ribbon-Shaped Pd Nanoparticle Assemblies by Spontaneous Organization. **2007**, 7666–7670.

(56) Imhof, A.; Pine, D. J. Ordered Macroporous Materials by Emulsion Templating. **1997**, *389*.

(57) Brust, M.; Walker, M.; Bethell, D.; Schiffrin, D. J.; Whyman, R. Synthesis of Thiol-Derivatised Gold Nanoparticles in. **2000**, 801–802.

(58) Fouetio Kengne, B.-A.; Karmakar, S.; Kaura, M.; Sai, V. V. R.; Corti, G.; Niraula, I. B.; Larin, A.; Hall, J.; Sowell, D.; Hrdlicka, P. J.; et al. Self-Assembled Monolayers of Thiols Adsorbed on Au/ZnO-Functionalized Silica Nanosprings: Photoelectron Spectroscopy-Analysis and Detection of Vaporized Explosives. *ACS Appl. Mater. Interfaces* **2014**, *6*, 13355–13366.

(59) Hinterwirth, H.; Kappel, S.; Waitz, T.; Prohaska, T.; Lindner, W. Terms of Use Quantifying Thiol Ligand Density of Self-Assembled Monolayers on Gold Nanoparticles by Inductively Coupled Plasma À Mass Spectrometry. **2013**, 1129–1136.

(60) Larson-Smith, K.; Pozzo, D. C. Pickering Emulsions Stabilized by Nanoparticle Surfactants. *Langmuir* **2012**, *28*, 11725–11732.

(61) Zeng, N.; Murphy, A. B. Heat Generation by Optically and Thermally Interacting Aggregates of Gold Nanoparticles under Illumination. *Nanotechnology* **2009**, *20*, 375702.

(62) Schatz, G.; Shuford, K. Optical Properties of Gold Nanospheres. **2005**, *2*, 27–33.

(63) Brûlet, A., Boue, F., Cotton, J. P. About the Experimental Determination of the Persistence Length of Wormlike Chains of Polystyrene. *J. Phys. II Fr.* **1996**, *6*, 885–891.

(64) Tam, A. C. Applications of Photoacoustic Sensing Techniques. *Rev. Medern Phys.* **1986**, *58*.

(65) Wilson, K.; Homan, K.; Emelianov, S. Biomedical Photoacoustics beyond Thermal Expansion Using Triggered Nanodroplet Vaporization for Contrast-Enhanced Imaging. *Nat. Commun.* **2012**, *3*, 618.

(66) Matsunaga, T. O.; Sheeran, P. S.; Luois, S.; Streeter, J. E.; Mullin, L. B.; Banerjee, B.; Dayton, P. a. Phase-Change Nanoparticles Using Highly Volatile Perfluorocarbons: Toward a Platform for Extravascular Ultrasound Imaging. *Theranostics* **2012**, *2*, 1185–1198.

(67) Frens, G. Controlled Nucleation for the Regulation of Particle Size in Monodisperse Gold Suspensions.pdf. *Nat. Phys. Sci.* **1973**, *241*, 20–22.

(68) Arnal, B.; Perez, C.; Wei, C.-W.; Lombardo, M.; Pelivanov, I.; Matula, T.; Pozzo, L.; O'Donnell, M. Sono-Photoacoustic Imaging of Gold Nanoemulsions: Part I. Exposure Thresholds. *Submitted*.

(69) Su, K.-H.; Wei, Q.-H.; Zhang, X.; Mock, J. J.; Smith, D. R.; Schultz, S. Interparticle Coupling Effects on Plasmon Resonances of Nanogold Particles. *Nano Lett.* **2003**, *3*, 1087–1090.

(70) Lu, L.; Luo, Z.; Xu, T.; Yu, L. Cooperative Plasmonic E Ff Ect of Ag and Au Nanoparticles on Enhancing Performance of Polymer Solar Cells. **2013**.